

1 **Alpacas in Space - An Autobiography**
2

3 By
4

5 JOSEPH LEVINE
6 DISSERTATION
7

8 Submitted in partial satisfaction of the requirements for the degree of
9
10 DOCTOR OF PHILOSOPHY

11 in
12

13 Physics
14

15 in the
16

17 OFFICE OF GRADUATE STUDIES
18
19 of the
20

21 UNIVERSITY OF CALIFORNIA
22

23 DAVIS
24

25 Approved:
26

27 J. Anthony Tyson, Chair
28

30 S. Mani Tripathi
31

33 Brian Kolner
34

36 Committee in Charge
37

38 2025

³⁹ Abstract

40 An Afghan, an Albanian, an Algerian, an American, an Andorran, an Angolan, an Antiguans,
41 an Argentine, an Armenian, an Australian, an Austrian, an Azerbaijani, a Bahamian, a
42 Bahraini, a Bangladeshi, a Barbadian, a Barbudans, a Batswanan, a Belarusian, a Belgian,
43 a Belizean, a Beninese, a Bhutanese, a Bolivian, a Bosnian, a Brazilian, a Brit, a Bruneian,
44 a Bulgarian, a Burkinabe, a Burmese, a Burundian, a Cambodian, a Cameroonian, a Cana-
45 dian, a Cape Verdean, a Central African, a Chadian, a Chilean, a Chinese, a Colombian, a
46 Comoran, a Congolese, a Costa Rican, a Croatian, a Cuban, a Cypriot, a Czech, a Dane,
47 a Djibouti, a Dominican, a Dutchman, an East Timorese, an Ecuadorean, an Egyptian, an
48 Emirian, an Equatorial Guinean, an Eritrean, an Estonian, an Ethiopian, a Fijian, a Fil-
49 ipino, a Finn, a Frenchman, a Gabonese, a Gambian, a Georgian, a German, a Ghanaian, a
50 Greek, a Grenadian, a Guatemalan, a Guinea-Bissauan, a Guinean, a Guyanese, a Haitian,
51 a Herzegovinian, a Honduran, a Hungarian, an I-Kiribati, an Icelander, an Indian, an In-
52 donesian, an Iranian, an Iraqi, an Irishman, an Israeli, an Italian, an Ivorian, a Jamaican,
53 a Japanese, a Jordanian, a Kazakhstani, a Kenyan, a Kittian and Nevisian, a Kuwaiti, a
54 Kyrgyz, a Laotian, a Latvian, a Lebanese, a Liberian, a Libyan, a Liechtensteiner, a Lithua-
55 nian, a Luxembourger, a Macedonian, a Malagasy, a Malawian, a Malaysian, a Maldivan, a
56 Malian, a Maltese, a Marshallese, a Mauritanian, a Mauritian, a Mexican, a Micronesian, a
57 Moldovan, a Monacan, a Mongolian, a Moroccan, a Mosotho, a Motswana, a Mozambican,
58 a Namibian, a Nauruan, a Nepalese, a New Zealander, a Nicaraguan, a Nigerian, a Nigerien,

59 a North Korean, a Northern Irishman, a Norwegian, an Omani, a Pakistani, a Palauan, a
60 Palestinian, a Panamanian, a Papua New Guinean, a Paraguayan, a Peruvian, a Pole, a
61 Portuguese, a Qatari, a Romanian, a Russian, a Rwandan, a Saint Lucian, a Salvadoran,
62 a Samoan, a San Marinese, a Sao Tomean, a Saudi, a Scottish, a Senegalese, a Serbian, a
63 Seychellois, a Sierra Leonean, a Singaporean, a Slovakian, a Slovenian, a Solomon Islander,
64 a Somali, a South African, a South Korean, a Spaniard, a Sri Lankan, a Sudanese, a Suri-
65 namer, a Swazi, a Swede, a Swiss, a Syrian, a Tajik, a Tanzanian, a Togolese, a Tongan,
66 a Trinidadian or Tobagonian, a Tunisian, a Turk, a Tuvaluan, a Ugandan, a Ukrainian, a
67 Uruguayan, a Uzbekistani, a Venezuelan, a Vietnamese, a Welshman, a Yemenite, a Zambian
68 and a Zimbabwean

69 all go to a bar..

70 The doorman stops them and says "Sorry, I can't let you in without a Thai."

71 Contents

72	Contents	iv
73	List of Figures	v
74	List of Tables	vii
75	1 The Dark Matter Story	3
76	2 Experiment Overview and Design	7
77	2.1 Sources of Power in Measured Spectrum	9
78	2.2 Toy Analysis	29
79	2.3 Thermal Noise in A Cavity	38
80	2.4 Reverberation Chambers and Statistical Uniformity	38
81	2.5 System Design	38
82	3 System Characterization and Data Acquisition	59
83	3.1 Control and Quantifying of Uncertainties	61
84	4 Data Analysis and Calibration	63
85	4.1 Hardware Injection Test	64
86	5 Beyond 300 MHz	79
87	Bibliography	80

⁸⁸ List of Figures

89	1.1	Expected vs observed velocity distributions of M33	4
90	1.2	Dark matter mass regimes	6
91	2.1	Blackbody electric field spectral density from radio to UV frequencies	11
92	2.2	An antenna and matched resistor in cavities which are in thermal equilibrium.	14
93	2.3	Simulated antenna noise voltage at room temperature in the time domain	16
94	2.4	Simulated antenna noise power spectral density at room temperature in the frequency domain	17
95	2.5	Effect of averaging on simulated antenna noise power spectral density at room temperature in the frequency domain	18
96	2.6	Schematic of LNA adding input referred noise	23
97	2.7	Schematic of cascade of amplifiers and their added noise	25
98	2.8	Cascaded noise temperature for system with two amplifiers	26
99	2.9	Input-referred power spectral density from simplified simulation	31
100	2.10	Noise spectrum containing sub-detection-threshold signal.	34
101	2.11	Noise spectrum containing sub-detection-threshold signal, various number of averages	36
102	2.12	XXXX	37
103	2.13	Schematic of the RF receiver system	39
104	2.14	Spectrum from veto antenna during 300MHz data run	42
105	2.15	Photo of set up to measure Shielding effectiveness of shielded room	43
106	2.16	Shielding effectiveness of shielded room, 50-300 MHz	44
107	2.17	Shielding effectiveness of shielded room, 125-3000 MHz	45
108	2.18	AB-900A biconical antenna free space effective aperture, simulated, measured and theoretical	47
109	2.19	simulated AB-900A biconical antenna free space complex input impedance, vs measured biconical data	48
110	2.21	Schematic of Interlock board	53
111	2.22	Photo of lead-acid battery and slow turn on circuit	54
112	2.23	Acquisition efficiency for GPU-based Real-time spectrum analyzer	56
113	3.1	Data stream of real time DAQ. This set up is duplicated for channels A and B .	61
114	3.2	Gain vs. voltage of front end amplifier	61

120	4.1	Schematic of hardware injection test	66
121	4.2	Average S parameters of hardware injection test	67
122	4.3	Histogram of frequencies used for hardware injection test	70
123	4.4	Output-referred power spectral density from the hardware injection test	72
124	4.5	Standard deviation on output-referred power spectral density from the hardware injection test	73
126	4.6	Standard deviation of output-referred power spectral density from the hardware injection test, computed with median absolute deviation	74
128	4.7	Output-referred power spectrum from hardware injection test, various levels of zoom	76
130	4.8	Normalized, output-referred power spectrum from hardware injection test, various levels of zoom	77
132	4.9	Matched filtered, output-referred power spectrum from hardware injection test, various levels of zoom	78
133			

¹³⁴ **List of Tables**

135	2.1	Caption	35
136	2.2	Specifications for the Pasternack PE15A1012-E. The voltage is regulated internally, so the exact voltage supplied is not critical	51
137			
138	2.3	Specifications for the miniCircuits ZKL-1R5+ The voltage is regulated internally, so the exact voltage supplied is not critical	52
139			
140	2.4	Specifications for the spectrum analyzer used for run 1A.	55

141

Acknowledgments

142 Thank you to: Ben

143 Dave Hemmer

144 Nathan IT

145 Monda

146 emiljia

147 Bill Tuck

148 Buchholtz/Ayars/Nelson/Kagan/Clare/Patrova/Rick Danner/pechkis

149 parents

150 janet/joel

151 baba/papa

152 Belva

153 chatGPT

154 Mr Keye

155 Bill Nye

156 Self plagiarism statement <https://journals.aps.org/copyrightFAQ.html>

157 As the author of an APS-published article, may I include my article or a portion
158 of my article in my thesis or dissertation? Yes, the author has the right to use
159 the article or a portion of the article in a thesis or dissertation without requesting
160 permission from APS, provided the bibliographic citation and the APS copyright
161 credit line are given on the appropriate pages.

162 <https://grad.ucdavis.edu/preparing-filing-your-thesis-or-dissertation>

163 Published or publishing pending material may be used with permission from the
164 copyright owner, if not you, and the Graduate Chair, if you are not the first-
165 author. See the Copyright FAQ for information about permissions when using
166 published material.

167 Material you have authored, and which has been previously published or is pend-
168 ing publishing, may be used in its published format with three exceptions: 1)
169 Margins - You must maintain 1" margins on all sides throughout the paper. 2)
170 Pagination - page numbers must follow the UC Davis standards. 3) The title
171 page must follow UC Davis standards and you must include an overall abstract.

172 comment: Need to add note about github and where code comes from

173

174 File: thesis.tex

175 Encoding: utf8

176 Sum count: 4797

177 Words in text: 3519

178 Words in headers: 78

179 Words outside text (captions, etc.): 1030

180 Number of headers: 19

181 Number of floats/tables/figures: 14

182 Number of math inlines: 162

183 Number of math displayed: 8

184 Subcounts:

185 text+headers+captions (#headers/#floats/#inlines/#displayed)

186 664+6+0 (2/0/0/0) _top_

187 369+4+71 (1/2/3/0) Chapter: The Dark Matter Story

188 310+4+0 (1/0/0/0) Chapter: Experiment Overview and Design

189 37+6+0 (1/0/0/1) Section: Sources of Power in Measured Spectrum

190 271+8+148 (3/1/47/6) Subsection: Thermal Noise

191 49+0+0 (0/0/24/0) Subsection: Dark Photon Signal

192 6+0+0 (0/0/3/0) Subsection: Radio Frequency Interference

193 30+0+0 (0/0/16/0) Subsection: Amplifier Chain Noise\codedir{thesis/ch2/CH2.ipynb}

194 6+0+0 (0/0/4/0) Subsection: ADC effects

```
195 18+0+0 (0/0/4/0) Section: Toy Analysis \codedir{thesis/ch2/toyAnalysis.ipynb}
196 22+0+0 (0/0/13/0) Subsection: Signal significance
197 9+0+0 (0/0/5/0) Subsection: Shielded room
198 2+0+0 (0/0/2/0) Subsection: Antenna
199 3+0+0 (0/0/1/0) Subsection: Terminator and fiber-optic switch control
200 11+0+0 (0/0/3/0) Subsection: Signal conditioning
201 0+0+0 (0/0/0/0) Subsection: Spectrum Analyzer Details
202 309+5+16 (1/1/3/0) Chapter: System Characterization and Data Acquisition
203 0+5+0 (1/0/0/0) Section: Control and Quantifying of Uncertainties
204 5+6+7 (1/1/0/0) Subsection: Direct Measurement of Amp Chain Parameters
205 233+4+0 (1/0/1/0) Chapter: Data Analysis and Calibration
206 77+7+0 (1/0/0/0) Section: Hardware Injection Test \codedir{daqAnalysisAndExperiments/r
207 752+13+391 (3/3/30/1) Subsection: Injection test prerequisites
208 241+4+265 (1/3/1/0) Subsection: Performing the injection test
209 89+3+132 (1/3/2/0) Subsection: Inspection of Data
210 6+3+0 (1/0/0/0) Chapter: Beyond 300 MHz
211
212 (errors:2)
```

²¹³ Chapter 1

²¹⁴ The Dark Matter Story

215

If we start making a list of
things that aren't here, we
could be here all night. You
know, pens for instance. Let's
stick with things we can see.

Wheatley

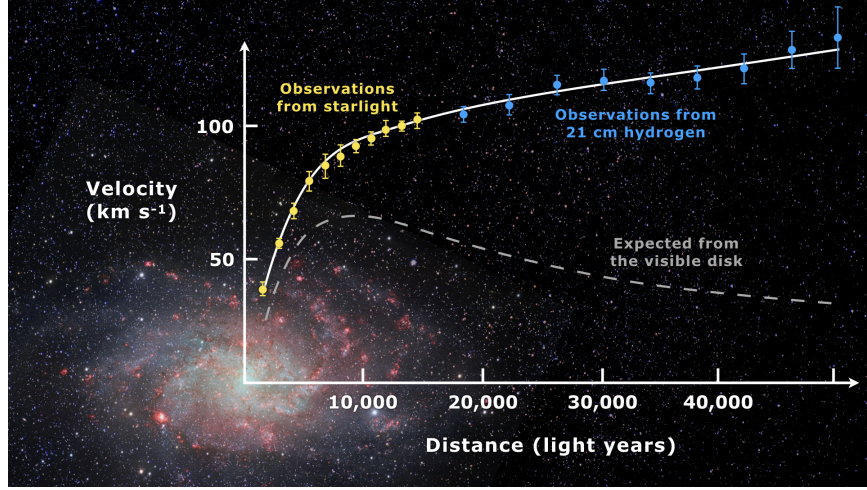


Figure 1.1: Expected vs observed velocity distributions of M33

216 It is believed that a large majority of the mass in the universe comes from an as yet
 217 undetermined source. This claim stems originally from work performed in 1933 by Fritz
 218 Zwicky who noticed a discrepancy between measured velocities of galaxies within the Coma
 219 Cluster and velocities predicted by applying the virial theorem. He wrote

220 *If this [experimental result] would be confirmed we would get the surprising result
 221 that dark matter is present in much greater amount than luminous matter [1].*

222 Vera Rubin furthered this work by measuring velocities of stars rotating in the M31
 223 galaxy and concluded there must be additional non-luminous mass (originally published in
 224 [2], and shown in Fig.1.1). Studies of other phenomena, such as lensing (see [**lensing2**]) have
 225 confirmed the existence of this dark matter, and it is currently one of the major mysteries
 226 in modern physics.

227 Since the 1980's, the leading theories have consisted of an unknown species of elementary

228 particle. The search for weakly interacting massive particles (WIMPs) have dominated
229 the budgets and schedules of the dark matter search effort but have yet to provide any
230 experimental evidence.

231 In light of this, the 2017 community report on dark matter [3] highlights a need for
232 a multi-experiment program in which many small scale experiments ($< \$10M$) split up to
233 cover the vast landscape of potential dark matter candidates (see Fig. 1.2). Since very
234 little is known about the dark matter, it is a playground for theoretical physicists to invent
235 candidates. This overwhelming search should be narrowed down.

236 The enormous mass range splits nicely into two regimes; waves and particles. At a mass
237 of order 1eV the inter-particle spacing \approx wavelength. Lighter than this it is more convenient
238 to think of dark matter as a wave. Alternatively, dark matter candidates heavier than this
239 are more conveniently modeled as exhibiting particle-like behavior. The Dark E-Field Radio
240 experiment searches for dark photons in the nano- to milli-eV mass range where dark matter
241 is best described as a wave. This property means one would search for a dark photon using
242 wave-like detectors, e.g. antennas.

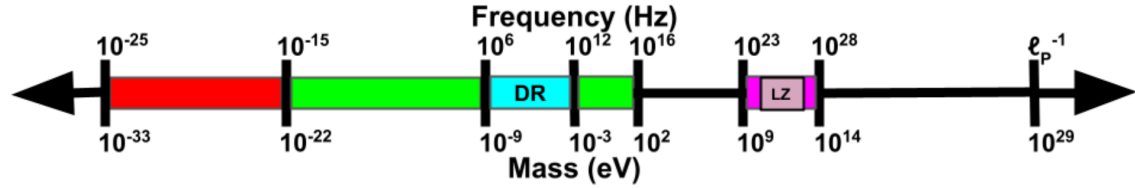


Figure 1.2: Cartoon depicting the mass scales over which dark matter may be found. Corresponding frequencies shown above. At heavy mass scales $> \mathcal{O}(1\text{ eV})$ the dark matter would behave like a particle, while on the lighter end it would behave like a wave. The Dark Radio Experiment searches at radio/microwave frequencies (blue) for a hidden photon using an antenna and spectrum analyzer. LUX-ZEPLIN Experiment (LZ) also shown.

²⁴³ Chapter 2

²⁴⁴ Experiment Overview and Design

245

A month in the laboratory can
often save an hour in the
library.

Frank Westheimer

246 Veljko Radeka said of detectors “One would imagine that in each particular case the
247 best solution is arrived at by 1) the detector design to maximize the significant signal, 2)
248 reduction of noise at its physical source, and 3) optimum filtering of signal and noise.” [4].
249 While he was referring to position sensitive particle detectors, the same three principles apply
250 to this experiment. Put more directly, the goal is to maximize the signal to noise ratio. The
251 detector in this case is a low-noise, wide-band radio receiver system searching not for discrete
252 instances of particle-like interactions, but for coherent waves which are constant over long
253 periods. The signal is a small excess of narrow-band, radio frequency power received by an
254 antenna in a cavity. The noise is the white, thermal background due to the 300 K walls. The
255 system is shown schematically in Fig. 2.13.

256 This chapter begins with a section titled Toy Analysis which walks through several back-
257 of-the-envelope calculations to follow the signal and noise as it progresses from fields in
258 free space through a simplified detector, resulting in a (simulated) dark photon detection.
259 Through this section, several important concepts will come up and their implications can be
260 analyzed. This will result in intuition which will explain the remaining design choices of Sec.
261 2.5. Furthermore, the actual experiment will report a null result, i.e. a lack of detection
262 of a signal on a background. By following a signal *forward* through the system and data
263 analysis, it will be more clear how to infer an exclusion limit from a power spectrum and
264 working *backward* through the experiment.

265 In the following two sections, 2.3 and 2.4, effects will be introduced that were not apparent
266 from the simplistic analysis of the first section. The final section, 2.5, details each piece of
267 the system.

268 **2.1 Sources of Power in Measured Spectrum**

269 This section will break down each term in the following equation for the input-referred power

$$P_i = \text{Thermal Noise} + \text{Dark Photon Signal} + \text{RFI} + \text{Amp Chain Noise} + \text{ADC Effects}/G, \quad (2.1)$$

270 where G is a gain factor. While convenient, this word equation is not rigorous, and relies
271 on the following subsections 2.1.1 - 2.1.5 for definition.

272 **2.1.1 Thermal Noise**

273 **2.1.1.1 Blackbody Electric Field Density**

274 This sub section estimates the noise-like¹ electric field in free space due to black body
275 radiation. It assumes to be in *some* enclosure in that the ambient temperature is known to
276 be 300 K and not the 3.6 K of the sky.

277 Planck's law gives the black body spectral energy density as

$$u_\nu(\nu, T) d\nu = \frac{8\pi h\nu^3}{c^3} \frac{1}{e^{h\nu/kT} - 1} d\nu \quad \left[\frac{J}{m^3} \right]. \quad (2.2)$$

278 This is frequently written in terms of spectral radiance,

$$B_\nu(\nu, T) d\nu = \frac{2h\nu^3}{c^2} \frac{1}{e^{h\nu/kT} - 1} d\nu d\Omega \quad \left[\frac{W}{m^2} \right]. \quad (2.3)$$

¹“Noise-like” simply means that the power contained in a signal is proportional to the bandwidth measured. Noise-like signals are more conveniently described as a power spectral density (PSD) which we will describe with the symbol S . As we will see, coherent signals which have finite width in frequency space $\Delta\nu_{\text{sig}}$ can share this property if the measurement bandwidth $\Delta\nu_{\text{RF}} \approx \Delta\nu_{\text{sig}}$, even though one wouldn't think of a coherent signal as being “noise-like”

279 Integrating this isotropic radiance over a solid angle 4π sr as well as a small frequency
 280 band $\Delta\nu$ gives the flux density $|\mathbf{S}|$ (AKA, the magnitude of the Poynting vector),

$$\begin{aligned} |\mathbf{S}| &= \int_0^{4\pi} \int_{\nu}^{\nu+\Delta\nu} B_{\nu}(\nu, T) d\nu d\Omega \\ &= \int_0^{4\pi} \int_{\nu}^{\nu+\Delta\nu} \frac{2h\nu^3}{c^2} \frac{1}{e^{h\nu/kT} - 1} d\nu d\Omega \quad \left[\frac{W}{m^2} \right] . \\ &\approx \frac{8\pi h\nu^3}{c^2} \frac{1}{e^{h\nu/kT} - 1} \Delta\nu \end{aligned} \quad (2.4)$$

281 The flux density can be related to the rms electric field from Poynting's theorem

$$|\mathbf{S}| = \frac{|E_{\text{rms}}|^2}{\eta} \quad \left[\frac{W}{m^2} \right], \quad (2.5)$$

282 where η is the impedance of free space. Equating Eqs. 2.4 and 2.5 and solving for the
 283 electric field gives

$$\frac{|E_{\text{rms}}|}{\sqrt{\Delta\nu}} = \sqrt{\eta \frac{8\pi h\nu^3}{c^2} \frac{1}{e^{h\nu/kT} - 1}} \quad \left[\frac{V}{m \cdot \sqrt{Hz}} \right], \quad (2.6)$$

284 and is plotted in Fig. 2.1.

285 Eq. 2.6 breaks up nicely into two regimes,

$$\frac{|E_{\text{rms}}|}{\sqrt{\Delta\nu}} = \begin{cases} \sqrt{\eta \frac{8\pi kT\nu^2}{c^2}} & \text{Rayleigh-Jeans regime } (h\nu \ll kT) \\ \sqrt{\eta \frac{8\pi h\nu^3}{c^2} e^{-h\nu/kT}} & \text{Wien approximation } (h\nu \gg kT) \end{cases} \quad \left[\frac{V}{m \cdot \sqrt{Hz}} \right]. \quad (2.7)$$

286 At frequencies and temperatures where the experiment is operated (< 300 MHz and
 287 300K), $h\nu/kT \lesssim 5 \times 10^{-5}$ suggesting the Rayleigh-Jeans approximation is valid. At 300 K,
 288 this yields electric field spectral densities of 1 and $6 nV/m\sqrt{Hz}$ at 50 and 300MHz respec-
 289 tively.

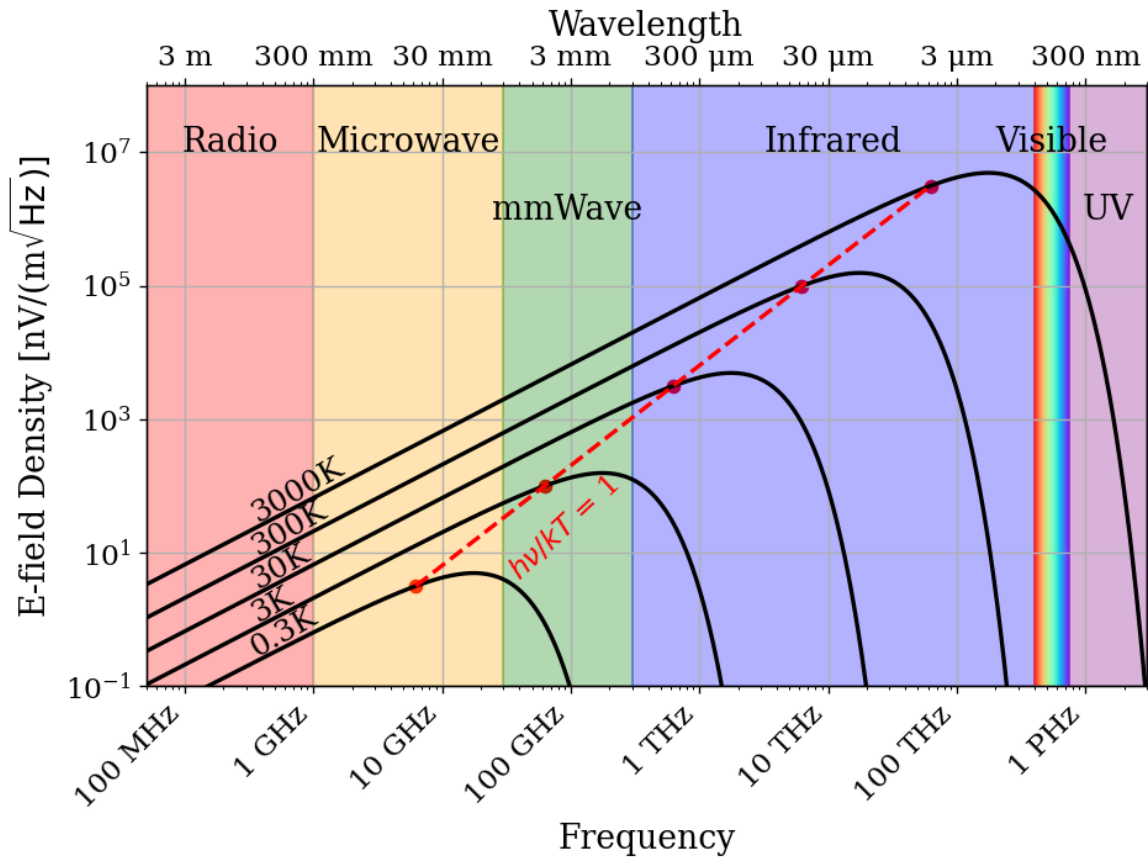


Figure 2.1: Blackbody electric field spectral density from radio to UV frequencies. A variety of temperatures are shown in black. The dashed red curve and red points indicate where along the black curves $h\nu = kT$, i.e. where Eq. 2.7 breaks up between the Rayleigh-Jeans regime to the Wien approximation. Note that these points are only a function of ν and T ; their vertical placement is chosen to lie on their respective curve but has no physical significance. The dark radio experiment is firmly in the Rayleigh-Jeans regime.

290 It is interesting to note, however, that for cryogenic experiments operating at a few GHz
 291 and in the sub K range, $h\nu/kT \approx 1$ and the full form of Eq. 2.6 must be used. This is shown
 292 at frequencies and temperatures to the right of the red dashed line in Fig. 2.1.

293 **2.1.1.2 Antenna Noise**

294 An antenna's effective aperture, A_e [m^2], represents the effective area that it has to collect

295 power density or irradiance [W/m^2] from an incident Poynting vector,

$$P_A = |\mathbf{S}|A_e, \quad (2.8)$$

296 Where $|\mathbf{S}|$ is the magnitude of the incident Poynting vector and P_r is the power received at
297 the antenna which is available at its terminals.

298 A_e is a directional quantity which varies with the antenna's directivity $D(\Omega)$, where Ω
299 represents solid angle around the antenna. It varies with frequency ν , though it is generally
300 discussed in terms of wavelength λ . Three matching parameters are introduced to describe
301 how much actual power the antenna is able to deliver to a transmission line; p the polarization
302 match of the wave to the antenna, m the impedance match of the antenna to the transmission
303 line and η_a the efficiency of the antenna which represents how much power is absorbed
304 compared to that lost to Joule heating of the antenna. p , m and η_a are all real, dimensionless
305 and vary between 0 and 1.

$$A_e \equiv \frac{\lambda^2}{4\pi} D(\Omega) p m \eta_a. \quad (2.9)$$

306 This definition follows [5], though some authors do not include p in the definition [6] [7].

307 A simple derivation of the direction-averaged effective aperture based on thermodynamics
308 will provide intuition. An isotropic antenna placed in a cavity at temperature T will be
309 illuminated by randomly polarized, isotropic radiation of the form given by the Rayleigh-

310 Jeans limit of Eq. 2.4, $|\mathbf{S}| = 8\pi kT\Delta\nu\nu^2/c^2$. The power received by the antenna can be found
 311 by Eq. 2.8,

$$\begin{aligned} P_A &= \langle A_e \rangle \frac{1}{2} |\mathbf{S}| \\ &= \langle A_e \rangle \frac{4\pi kT\nu^2}{c^2} \Delta\nu, \end{aligned} \quad (2.10)$$

312 Where the factor of $1/2$ is introduced to account for the random polarization and the $\int d\Omega$
 313 indicate an average aperture over all angles around the antenna. If an resistor is placed in a
 314 second cavity, also at temperature T , by it will deliver

$$P_R = kT\Delta\nu \quad (2.11)$$

315 into a matched transmission line. This is shown in Fig. 2.2. The second law of thermo-
 316 dynamics makes a very powerful statement here; the net power flow must equal 0 if the two
 317 temperatures are indeed equivalent. This means $P_R = P_A$ or Eq. 2.10 = Eq. 2.12,

$$\begin{aligned} \langle A_e \rangle \frac{4\pi kT\nu^2}{c^2} \Delta\nu &= kT\Delta\nu \\ \langle A_e \rangle &= \frac{c^2}{4\pi\nu^2} \quad [\text{m}^2] \\ &= \frac{\lambda^2}{4\pi} \end{aligned} \quad (2.12)$$

318 This allows us to conclude that the power spectral density S_{ant} received by an antenna
 319 surrounded by an isotropic temperature is simply $kT\Delta\nu$ in the Rayleigh-Jeans limit of room
 320 temperatures and standard electronic frequencies. This gives a power which is equivalent to
 321 the well known result for a resistor at 290 K,

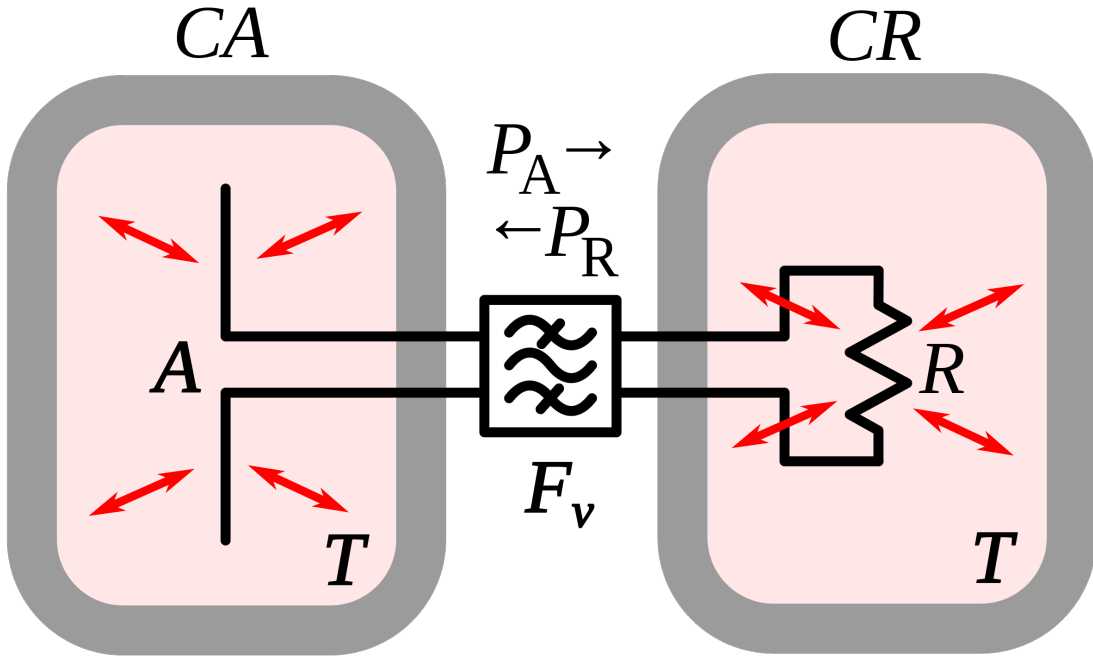


Figure 2.2: An antenna and matched resistor in cavities which are in thermal equilibrium. They are connected by a narrow filter permitting a narrow frequency band $\Delta\nu$.
Image from Wikipedia.

$$S_{\text{ant}} = 3.9 \times 10^{-22} [\text{W}/\text{Hz}] = -174 [\text{dBm}/\text{Hz}]. \quad (2.13)$$

322 Note that S_{ant} indicates power spectral density and should not be confused with \mathbf{S} which

323 indicates a Poynting vector.

324 2.1.1.3 Dicke radiometer equation

325 Equation 2.13 gave the mean of a power spectrum which is inherently noisy. We will now

326 show the origin of this spectrum.

327 An enclosure who's electrically-lossy walls contain free charge carriers at finite temper-

ature will radiate incoherently by the fluctuation dissipation theorem. This theorem is the underlying principal of phenomena such as Brownian motion [8] and Johnson-Nyquest noise [9], but was not generally proven until 1951 by Callen and Wellton [10]. The random thermal fluctuation of the charge carriers will radiate a black body spectrum. Observing the electric field in the time domain, one can imagine the radiation arriving at a detector at a wide variety of random frequencies and phases. This is incoherent noise in that at each time domain sample is independent of the one proceeding it ². The detector will produce a voltage which can be modeled as a Gaussian with zero mean and standard deviation $\sigma = \sqrt{S_{\text{ant}} \Delta \nu_{\text{RF}} |Z|}$ where Z is the system impedance (here 50Ω). This is shown for a room temperature antenna (or equivalently a room temperature resistor, see Fig. 2.2) in Fig. 2.3.

²The hidden assumption here is that blackbody radiation is totally incoherent. It actually has a coherence time $\tau_c \approx 2 \times 10^{-14} \text{ s}$ at 300 K [11]. For this statement to hold, the sample time $\tau_s \gg \tau_c$. For run 1A, $\tau_s = 1/800 \text{ MHz} = 1.25^{-9} \text{ s}$, 5 orders of magnitude more than τ_c

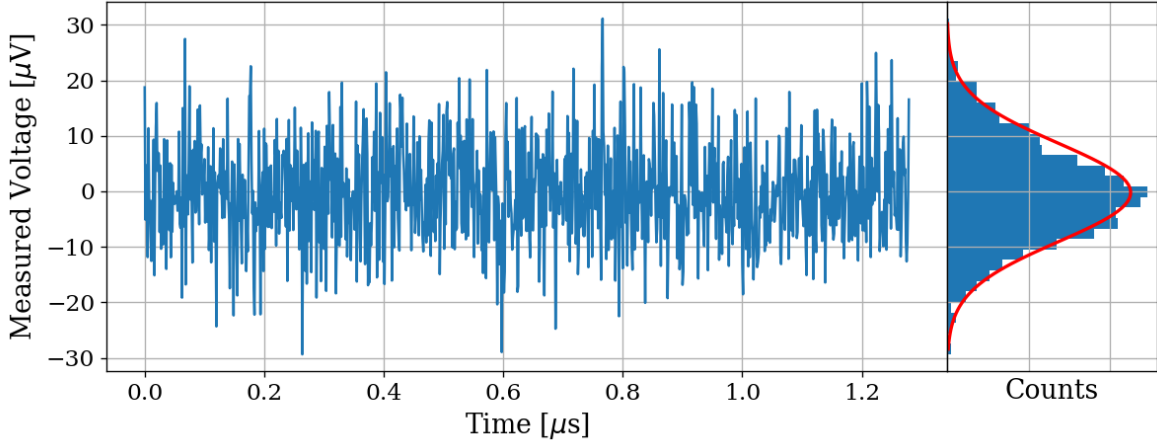


Figure 2.3: Simulated antenna noise voltage at room temperature in the time domain. Sample rate $\nu_s = 800\text{MHz}$ and number of samples $N = 2^{10} = 1024$. Bin width $\Delta\nu_{\text{RF}} = \nu_s/N \approx 800\text{ kHz}$. Data are binned and plotted as a histogram to the right. Best fit Gaussian is shown on the histogram in red with $\mu = -0.199\text{ }\mu\text{V}$ and $\sigma = 8.86\text{ }\mu\text{V}$. Counts have been normalized such that the bins add up to unity.

338 The next step in converting this time domain voltage signal to a frequency domain
 339 power spectral density (PSD). The first step is taking a discrete Fourier transform. This is
 340 usually implemented with an algorithm known as a fast Fourier transform (FFT), so that
 341 $\tilde{V} = \text{FFT}(V)$. In order to convert to a power spectrum, a non-trivial normalization prefactor
 342 must be included;

$$S = \frac{2}{N^2 |Z|} |\Re(\tilde{V})[:N//2]|^2, \quad (2.14)$$

343 where N is the number of samples, Z is the system impedance, and [:N//2] is python notation
 344 for the second half of the samples contained in the \tilde{V} array. Performing this operation on
 345 the data in Fig. 2.3 yealds the data in Fig. 2.4

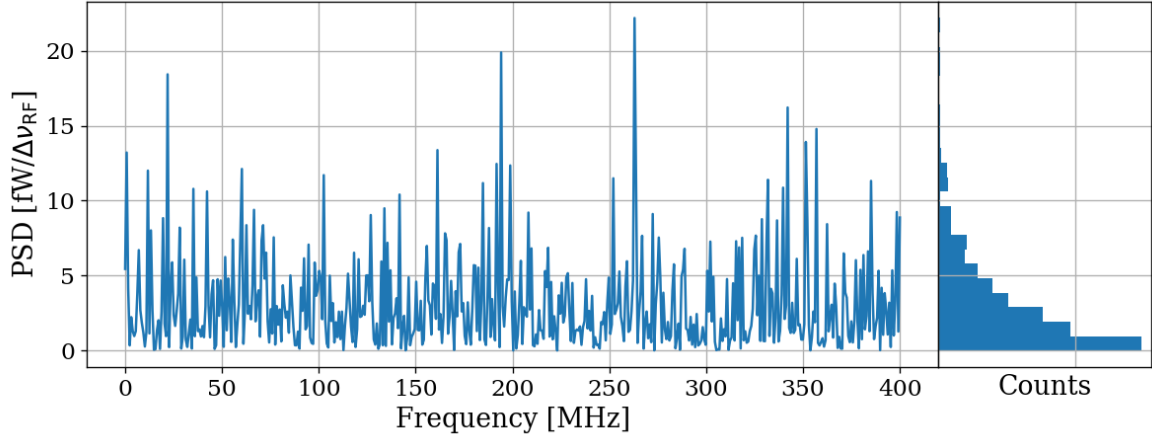


Figure 2.4: Simulated antenna noise power spectral density (PSD) at room temperature in the frequency domain. Sample rate $\nu_s = 800\text{MHz}$ and number of samples $N = 2^{10} = 1024$. Bin width $\Delta\nu_{\text{RF}} = \nu_s/N \approx 800\text{ kHz}$. Data are binned and plotted as a histogram to the right. Counts have been normalized such that the bins add up to unity.

346 The peculiar PDF of the histogram shown in Fig. 2.4 is known as a χ^2 distribution with
 347 1 degree of freedom and comes about because power is a positive-definite quantity and the
 348 standard deviation of the PSD is greater than it's mean.

349 However, by averaging many of the these power spectra together the central limit theorem
 350 dictates that we can expect the resulting PDF to be Gaussian. The transition from χ^2 to
 351 Gaussian distributed spectra is shown in Fig. 2.5.

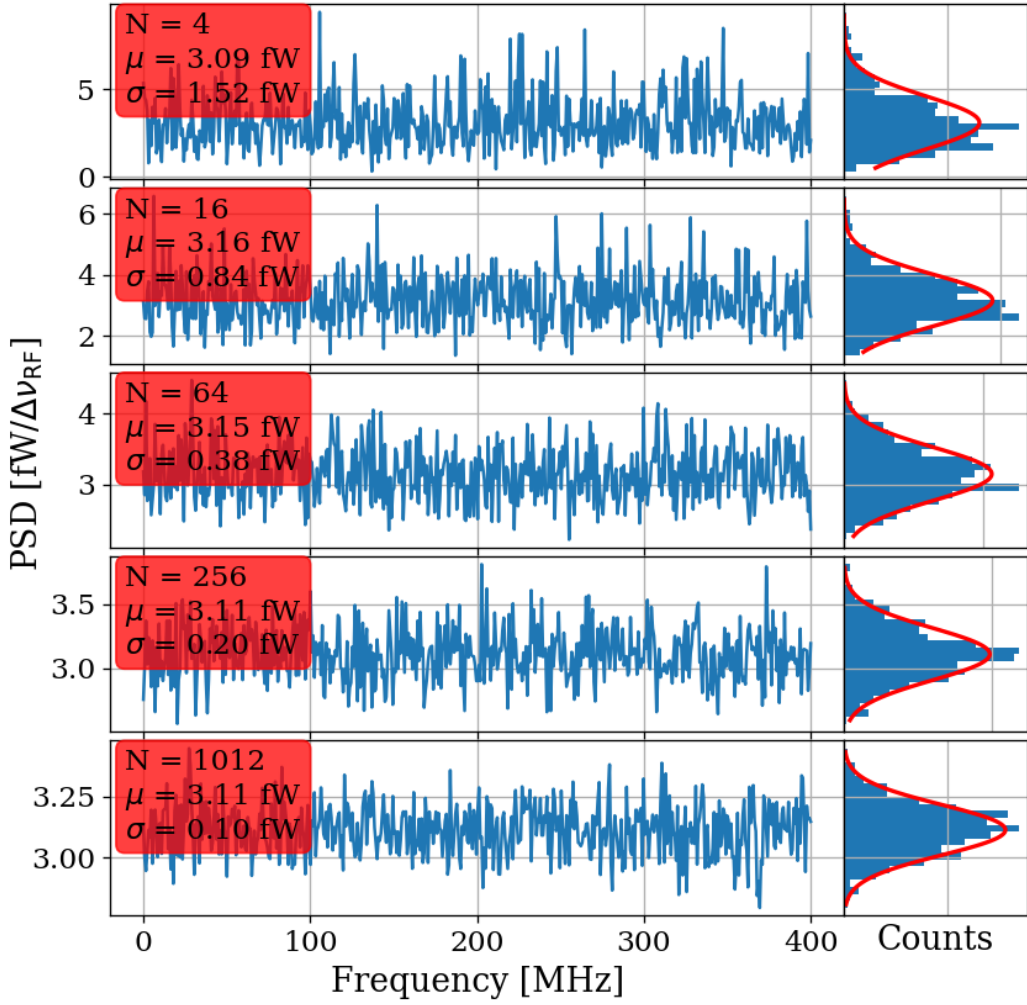


Figure 2.5: Effect of averaging on simulated antenna noise power spectral density (PSD) at room temperature in the frequency domain. Subplots show different number of averaged power spectra from $N = 4$ to 1024. Each subplot shows a factor of 4 times more averaging than the previous one. The Dicke radiometer equation predicts the standard deviation σ will scale like $N^{-1/2}$, once a large number of averages have been taken such that $\sigma \ll \mu$. Sample rate $\nu_s = 800\text{MHz}$ and number of samples $N = 2^{10} = 1024$. Bin width $\Delta\nu_{\text{RF}} = \nu_s/N \approx 800 \text{ kHz}$. Data are binned and plotted as a histogram to the right with a best fit Gaussian shown in red. Counts have been normalized such that the bins add up to unity. Note that the Y axis scale changes between sub plots to show the improvement of the Gaussian fit. The standard deviation is indeed decreasing between plots.

352 Finally, this averaged power spectrum can be modeled with the Dicke radiometer equa-
353 tion. The measured power (assuming only thermal noise) is given by

$$P_{\text{ant}} = kT\Delta\nu \left(1 \pm \frac{1}{\sqrt{\Delta\nu\tau}} \right) \quad [\text{W}]. \quad (2.15)$$

354 Here τ is the total acquisition time and so $\Delta\nu\tau$ is equivalent to the number of spectra
355 that are averaged together. This can be nondimensionalized and written

$$\frac{P_{\text{ant}}}{kT\Delta\nu_{\text{RF}}} = 1 \pm \frac{1}{\sqrt{N}} \quad [\text{W}], \quad (2.16)$$

356 which will become important during data analysis which is the topic of Ch. 4.

357 For the remainder of this thesis, unless otherwise stated, it will be assumed enough
358 spectra have been averaged together that a PSD is Gaussian and scales with the square root
359 of total acquisition time according to Eq. 2.15.

360 Thus far the analysis has focused only on thermal noise, however there are other sources
361 of noise and interfering signals which must be considered, not to mention the actual dark
362 photon signal.

363 2.1.2 Dark Photon Signal

364 The electric field of a kinetically mixed dark photon in free space $\mathbf{E}_{\text{ant}}^{\text{free space}}$ was derived in
365 Sec. [add reference: XXX](#). In a cavity, the E-field will be enhanced by the quality factor Q of
366 the cavity. This Q must be measured or simulated, but for this toy analysis we will assume

367 it to be known³. The E-field inside the cavity then is

$$\mathbf{E}_{\text{ant}} = \mathbf{E}_{\text{ant}}^{\text{free space}} \sqrt{Q}, \quad (2.17)$$

368 since Q is proportional to power, i.e. \mathbf{E}^2 . This E-field will then need to be converted from
369 a wave in the cavity to a wave in a 50Ω transmission line by an antenna. Similar to the
370 thermal noise of the previous section, this electric field will be converted via the effective
371 aperture of the antenna. Similar to Q , aperture will be assumed to be known.

372 The total received power from a coherent signal inside the room then is

$$P = \frac{\mathbf{E}_{\text{ant}}^{\text{free space}^2}}{\eta} Q < A_e >, \quad (2.18)$$

373 where η is the impedance of free space.

374 The observed spread of the frequencies of the dark photon are in important effect which
375 determine system design. In the following paragraphs of this section, several sections of
376 Gramolin et al. [13] are summarized, and the wording changed from “axion” to “dark
377 photon” where appropriate, as well as a few variables slightly renamed to better match
378 Levine et. al [add reference: levine et al.](#) Also note that the original calculation for the
379 predicted line shape this appears to be Michael Turner in 1990 [14].

380 A simple model of the dark photon line assumes it is monochromatic, i.e. it's line shape
381 is a delta function in frequency domain,

$$\nu_{\text{obs}} = \delta(\nu - \nu_{\text{DP}}). \quad (2.19)$$

382 This is consistent with it's production [add reference: misalignment mechanist/ch 1](#). How-

383 ever, when observed in a frame other than it's rest frame, the frequency of a (signal) dark

³Typical values are in the ball park of 100. Some experiments have ultra-high Q cavities $\approx 10^{10}$ [12]

384 photon will shift by an amount proportional to it's kinetic energy

$$\nu_{\text{obs}} = \left(1 + \frac{v_n^2}{2c^2}\right) \nu_{\text{DP}}, \quad (2.20)$$

385 where ν_{obs} is the observed frequency of the n th dark photon, v_n is it's velocity, c is the speed
386 of light, and ν_{DP} is it's rest frequency. The end result will be a signal that has some spread
387 in frequency, $\nu_{\text{DP}}/(\Delta\nu) \equiv Q_{\text{DP}} \approx 10^6$, with a line shape given by 2.23.

388 By summing over an infinity of dark photons of random phases and velocities (sampled
389 from the relative velocity of the dark matter halo), each with a frequency given by Eq. 2.20,
390 one can construct a power spectral density (PSD) of the dark photon signal as measured on
391 earth, S [W/Hz].

392 When performing a measurement, one records the voltage V emerging from a detector
393 for a period of time greater than the coherence of the dark photon $\tau_{\text{FFT}} \gg \tau_c$. The Fourier
394 transform of $V(t)$ is denoted $\tilde{V}(\nu)$

395 The signal will have a total power

$$P_0 = \frac{1}{\tau_{\text{FFT}}} \int_0^{\tau_{\text{FFT}}} \frac{|V(t)|^2}{|Z|} dt = \int_0^{1/\tau_{\text{FFT}}} S(\nu)^2 d\nu, \quad (2.21)$$

396 which is a statement of Parseval's theorem.

397 The normalized line shape is defined by dividing by P_0 ; $\lambda(\nu) \equiv S(\nu)/P_0$. This has the
398 property of being normalized to unity,

$$\int_0^\infty \lambda(\nu) d\nu = 1. \quad (2.22)$$

399 Finally, the result for this normalized line shape is

$$\lambda(\nu) = \frac{2 c^2}{\sqrt{\pi} v_0 v_{\text{lab}} \nu_{\text{DP}}} \exp \left(-\frac{\beta^2 v_0^2}{4 v_{\text{lab}}^2} - \frac{v_{\text{lab}}^2}{v_0^2} \right) \sinh \beta \quad \left[\frac{1}{\text{Hz}} \right], \quad (2.23)$$

400 where $|v_0| \approx 220$ km/s is the circular rotation speed of the Galaxy at the radius of the sun
401 (approximately 8 kpc), $v_{\text{lab}} \approx 233$ km/s is the relative velocity of the Sun to the rest frame
402 of the Galaxy and

$$\beta \equiv \frac{2 c v_{\text{lab}}}{v_0^2} \sqrt{\frac{2 (\nu - \nu_{\text{DP}})}{\nu_{\text{DP}}}}.$$

403 Equation 2.23 is plotted in Fig. [add reference: line shape in toy analysis](#). Note it's
404 quality factor $Q_{\text{DP}} \approx 10^6$ as mentioned above.

405 2.1.3 Radio Frequency Interference

406 Radio Frequency Interference (RFI) includes any coherent interfering signals which can be
407 detected by the experiment. While noise is better described as a power spectral *density*
408 [W/Hz] or electric field *density* [V/(m $\sqrt{\text{Hz}}$)], RFI is made up of more narrow lines and is
409 discussed in terms of a power [W] or electric field [V/m]. In this experiment, RFI is mitigated
410 through the shielding effectiveness (SE) of the cavity. SE measurements and more details
411 about local RFI are discussed further in Sec. 2.5.1, and a plot of the local RFI spectrum is
412 shown in Fig. 2.14.

413 The peak RFI spike is at 186 MHz and approximately 100 $\mu\text{V}/\text{m}$, an energy density
414 of roughly 10^{-11} W/m². This will be reduced by the SE of the room (roughly 120 dB at
415 200MHz, see Fig. 2.15), but just like a coherent dark photon, it will be enhanced by the

416 Q/effective aperture. This will be right on the edge of detection, but in the actual date run
 417 it was not detected.

418 **2.1.4 Amplifier Chain Noise⁴**

419 Any amplifier will have some noise which it adds to an incoming signal which will degrade
 420 the signal to noise ratio (SNR) of the measurement ⁵. A low noise amplifier (LNA) is an
 421 amplifier which has been specifically designed to minimize the noise contribution. This
 422 process is shown schematically in Fig. 2.6.

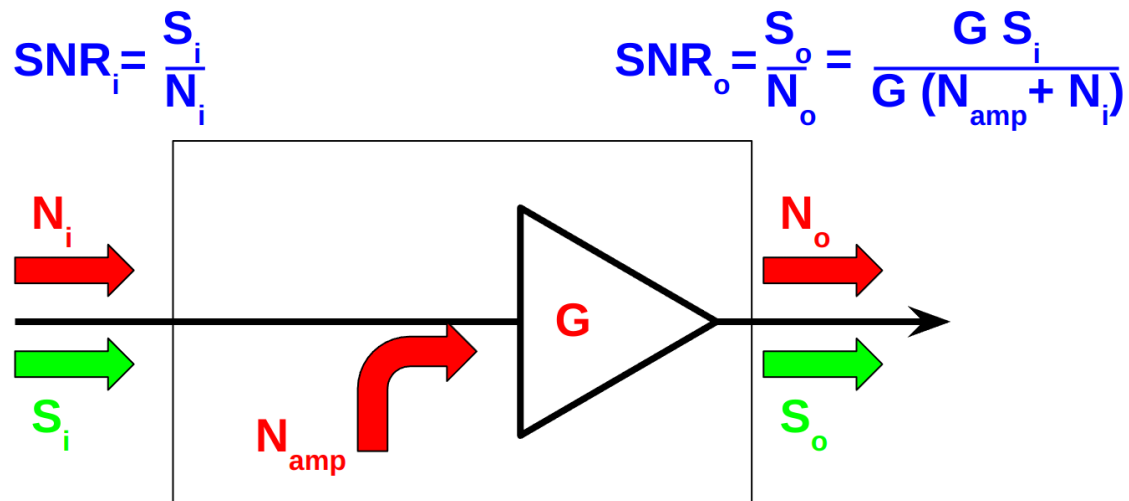


Figure 2.6: Schematic of LNA adding input referred noise N_{amp} . Since N_{amp} is referred to the input, it can be directly added to the input noise which is itself input-referred. The amplifier (depicted as a triangle) is assumed to be noiseless, while the physical amplifier including noise is contained in the rectangle.

⁴Code for this section can be found at: <https://github.com/josephmlev/darkRadio/tree/master/thesis/ch2/CH2.ipynb>

⁵A great lecture on the subject by Prof. Greg Durgin can be found at [15]

423 The performance of an LNA is generally evaluated by a figures of merit and noise factor
 424 (F). F is defined to be the ratio the SNR at the input of an LNA to that at its output.

$$\begin{aligned}
 F &\equiv \frac{\text{SNR}_i}{\text{SNR}_o} \\
 &= \frac{S/N}{[S G]/[(N + N_{\text{amp}})G]} \\
 &= \frac{1}{1/[1 + N_{\text{amp}}/N]} \\
 &= 1 + \frac{N_{\text{amp}}}{N},
 \end{aligned} \tag{2.24}$$

425 where S and N are the signal and noise [W] presented to the LNA respectively, N_{amp} is the
 426 input-referred noise added by the LNA and G is the gain. By factoring out the implicit $k \Delta\nu$
 427 from $N = kT\Delta\nu$, we find

$$F = 1 + \frac{T_e}{T_0}, \tag{2.25}$$

428 where T_e is the noise temperature of a device and T_0 the temperature of the system being
 429 measured by the LNA.

430 Note that following the same derivation as Eq. 2.24, it is simple to show that the noise
 431 figure of an attenuator at temperature T with loss L is given by

$$F_{\text{att}} = 1 + \frac{(L - 1)T}{T_0}, \tag{2.26}$$

432 where T_0 is the reference temperature defined above. If $T = T_0$, Eq. 2.26 simplifies to
 433 $F_{\text{att}} = L$

434 In order to standardize device specifications for across system applications, it is common
 435 to choose a reference temperature T_0 of 290K. If not specified, it is generally safe to assume
 436 this has been done.

437 Noise factor is simply defined from noise figure,

$$\text{NF} \equiv 10\log_{10}(F). \quad (2.27)$$

438 When working with LNAs, all three measurements (T_e , F and NF) are frequently used
 439 and one must use Eqs. 2.25 and 2.27 to convert between them.

440 One important generalization is that of a cascaded series of amplifiers, shown schemati-
 441 cally in Fig. 2.7.

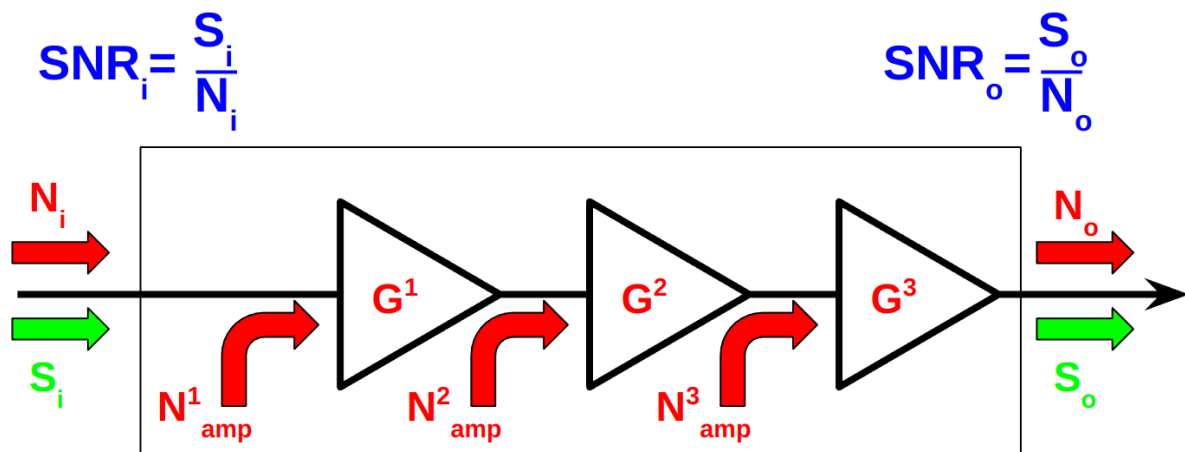


Figure 2.7: Schematic of cascade of $n = 3$ amplifiers and their added noise N_{amp}^n . Each amplifier has a gain of G^n . The SNR at the output is derived in Eq. 2.28. Note that superscripts in the figure and caption refer to index of each component and are not exponents.

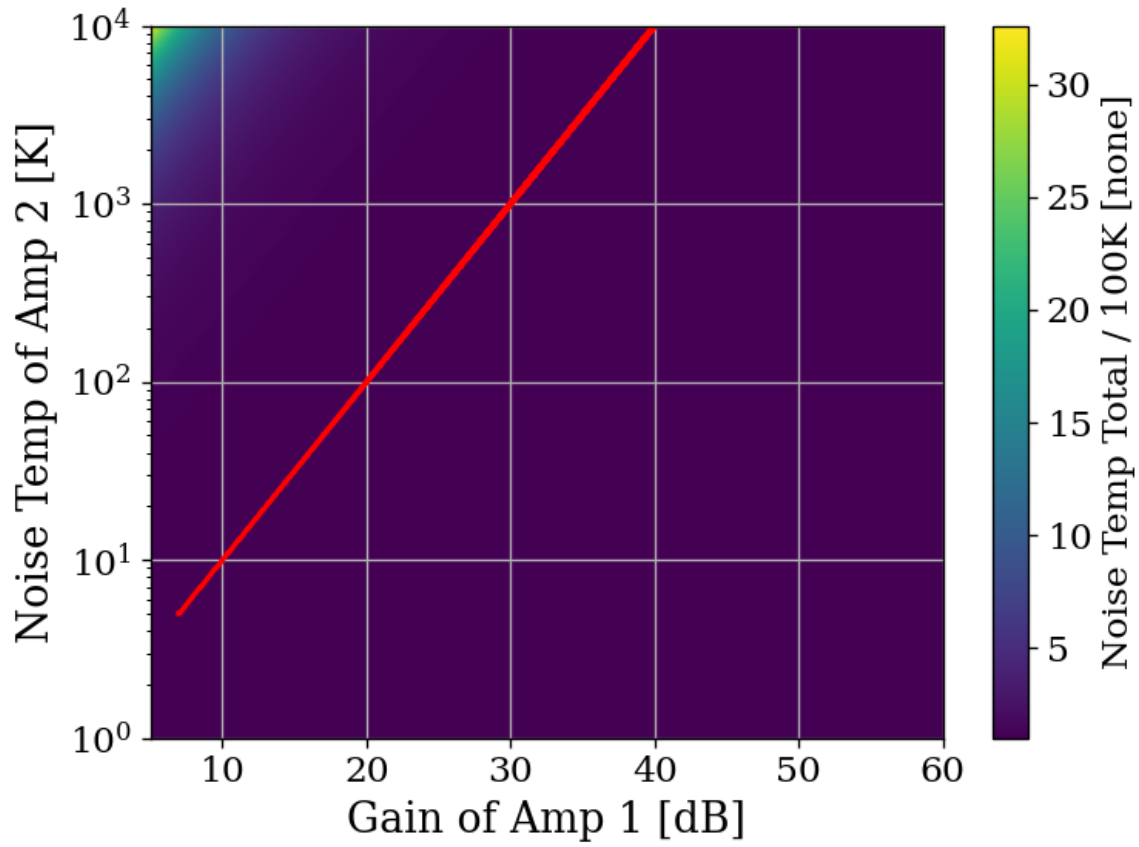


Figure 2.8: Cascaded noise temperature for system with $n = 2$ amplifiers, normalized to noise temperature of amplifier 1 (the so called LNA) = 100 K. Shown schematically (for $n = 3$) in Fig. 2.7. First amplifier's noise temperature and gain (40 dB and 100 K respectively) roughly equivalent to the LNA used in phase 1A of the experiment[16]. Red curve shows where the system's noise temperature is 1% higher than LNA noise temperature. This shows that for a 40 dB, 100 K LNA, in order to change the system noise temperature by 1 K, a second stage amplifier with a noise temperature of 10^4 would be required. Secondary amplifiers with noise temperatures closer to 500 K are realistic and inexpensive. Note that red curve should continue, but is cut off as a plotting artifact.

442 Here the total noise figure of n amplifiers can be shown to be

$$F_{\text{total}} = F_1 + \frac{F_2 - 1}{G_1} + \frac{F_3 - 1}{G_1 G_2} + \cdots + \frac{F_n - 1}{G_1 G_2 \cdots G_{n-1}}, \quad (2.28)$$

443 following the same derivation as Eq. 2.24. Since the noise temperature of a system depends

444 on the noise temperature a given amplifier divided by he gain which precedes it, a front-end
445 LNA with modest gain ensures the total noise figure of the the system is equal to it's noise
446 figure to very good approximation. This is shown in Fig. 2.8. We will use this approximation
447 and assert

$$\text{Amp Chain Noise} = \text{LNA Noise}, \quad (2.29)$$

448 Where LNA here is taken to mean the first gain stage in the amplifier chain
449 Noise figures are typically frequency dependant, though they vary slowly over frequency
450 and can be approximated as constant over narrow frequency bands. Noise figures are typically
451 given on the data sheet of the LNA [16], but can also be measured. Measurement of LNA
452 noise is covered in Sec. [add reference: ch 3](#) and is shown in Fig. [add reference: LNA NF](#)
453 (which is in good agreement with the LNA's data sheet [16]).

454 The power contributed by the LNA's noise is simply given by

$$P_{\text{LNA}} = kT_e\Delta\nu \quad (2.30)$$

455 This is again the mean of a fluctuating power, just as 2.15.

456 2.1.5 ADC effects

457 “ADC effects” is a catch all term which refers to power introduced by an analog-to-digital
458 converter. It contains are a three components, listed in order of importance;

$$\text{ADC Effects} = \text{Spurious Signals} + \text{ADC Noise Floor} \quad (2.31)$$

459 Equation 2.28 shows that gain G introduced before a noisy element in the RF chain, will
460 reduce the relative contribution of that noise by a factor of G . The same idea applies to
461 ADC effects, though one must be careful with the language used to describe this; spurious
462 *signals* are not noise, and the experiment's output *is* mostly noise.

463 **2.1.5.1 Spurious signals**

464 Spurious signals (also known as spurs) are coherent signals which are introduced into the
465 signal at the ADC⁶. They are likely caused by RFI due to various clocks in the PC in
466 close proximity to the ADC. The coherence of spurs means they will pop up above the noise
467 with more averaging. Spurs don't degrade the SNR of the experiment in the same way a
468 noisy amplifier chain would; they produce false positive candidates which must be excluded,
469 similar to RFI discussed in Sec. 2.1.3. Similar to ADC noise, they can be measured easily
470 by terminating the input of the ADC and scanning. They are investigated thoroughly in
471 Sec. [add reference: spur testing, ch 3](#), where they are shown to be nearly negligible, having
472 been mitigated by the gain of the system. There is a single spur detected after a few days
473 (see sec [add reference: fasle positive](#)), but for this simple analysis we will assume spurs are
474 negligible.

⁶Note that these spurs described here are not the same as the spurs that are described by the ADC specification *spur free dynamic range* (SFDR). SFDR is measured in dBc, i.e. *relative* to a carrier. Since our "carrier" is broadband noise, each bin produces some spurs which are -66 dBc [17] relative to itself. These spurs are also broadband, and average down with the experiment's noise. The SFDR spurs are negligible

475 **2.1.5.2 ADC noise**

476 ADC noise can simply be measured by terminating the input and taking a scan. This is
477 shown in Fig. [add reference: terminated input](#). The result is that ADC noise is a factor of
478 10^5 lower than the thermal noise of the experiment, both output-referred⁷, which agrees with
479 the ADC's data sheet [17]. Since ADC noise follows the same scaling as the experiment's
480 thermal noise (Eq. 2.15), this factor of 10^5 is independent of averaging, and ADC noise is
481 totally negligible.

482 **2.2 Toy Analysis**⁸

483 With each of the terms of Eq. 2.1 defined in the previous section, we will now perform and
484 view several simulations of a simplified dark photon signal on a simplified background. This
485 section should provide intuition about the process of detecting a weak, narrow signal on a
486 background PSD of thermal noise. It is assumed the noise has been averaged a sufficient
487 number of times such that it's PDF is Gaussian (discussed in Sec. 2.1.1.3). Furthermore,
488 following the discussion of Sec. 2.1, Eq. 2.1 can be simplified by setting RFI and ADC
489 Effects to zero and combining Thermal Noise (300 K) with Amp Chain Noise (100 K) into a
490 single term which represents the total of the noise in the whole system, $S_{\text{sys}} = P_{\text{sys}}/\Delta\nu_{\text{RF}} =$

⁷Technically it doesn't matter where they are referred since they are taken in ratio. As long as they are referred to the same point!

⁸Code for this section can be found at: <https://github.com/josephmlev/darkRadio/tree/master/thesis/ch2/toyAnalysis.ipynb>

491 $k(T_{\text{ant}} + T_{\text{LNA}})$. With these simplifications, the input-referred measured power is given by

$$P_{\mathbf{i}} = P_{\text{DP}} + kT_{\text{sys}}\Delta\nu_{\text{RF}} \left[1 \pm \frac{1}{\sqrt{N}} \right], \quad (2.32)$$

492 where $T_{\text{sys}} \equiv 400$ K, realistic for the experiment that is being simulated. Also note that this
493 equation assumes the dark photon's line shape is much more narrow than $\Delta\nu_{\text{RF}}$ such that the
494 measured input-referred dark photon power is independent of $\Delta\nu_{\text{RF}}$. In the simulations the
495 line shape will be modeled as a delta function as in Eq. 2.19. The signal will be introduced
496 simply by adding some power in a single bin to a Gaussian background in frequency domain.

497 Performing an FFT on a perfect (discretized) sine wave can cause it's power to be split
498 among adjacent bins depending on the ratio of the sample rate to the sine wave's frequency.

499 This can be minimized by windowing the time-domain data as is discussed in Ch. 2 Sec.
500 2 of Ben Godfrey's thesis [18]. This effect is avoided by working in the frequency domain and
501 adding power to a single bin which is the method used here. A reminder that throughout
502 this thesis, code is available at github and is linked in the footnote of each section title.

503 With a simple simulation framework in place, we can now begin to generate signals
504 containing-spectra. Figure 2.9 qualitatively shows the 400 K system noise (input-referred
505 antenna plus LNA) averaging down, leaving a small signal visible. Further subsections in
506 this section will quantify this.

507 With a basic conceptual framework in place, it is now simpler to quantify signal detection
508 and the uncertainty on how many averages are required to detect a signal, and have that
509 detection be significant in that it isn't a random fluctuation (false positive).

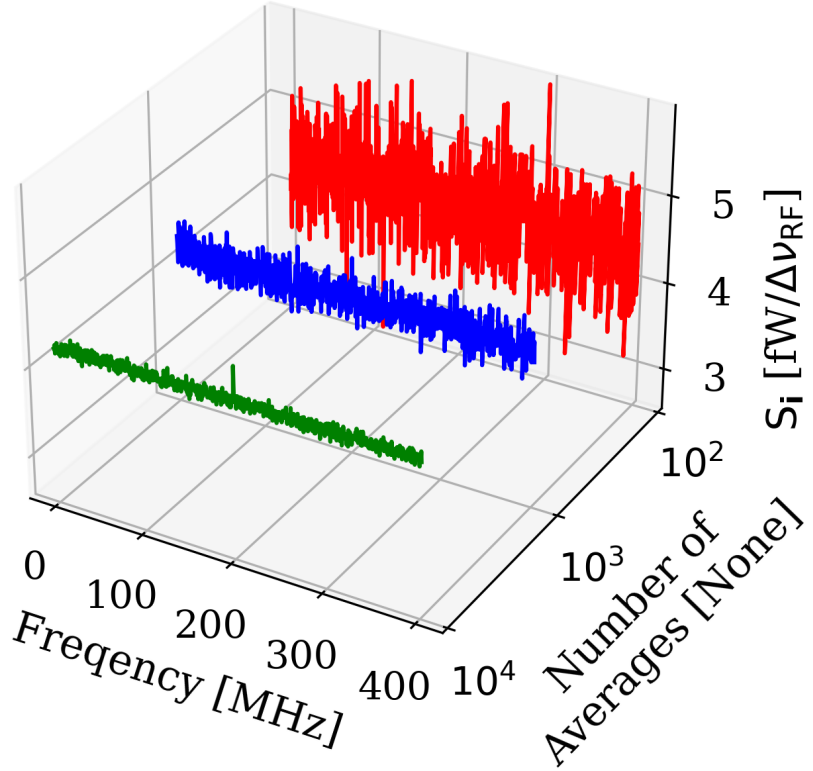


Figure 2.9: Input-referred power spectral density from simplified simulation illustrating noise averaging down to reveal a persistent, software-injected, dark photon proxy signal. The power of the signal P_{DP} is set to 0.4 fW and it only occupies a single bin. The mean of the noise is $\approx 4.3 \text{ fW}/\Delta\nu_{RF}$ where $\Delta\nu_{RF} \approx 0.78 \text{ MHz}$. The standard deviation ranges between $0.41 \text{ fW}/\Delta\nu_{RF}$ and $0.041 \text{ fW}/\Delta\nu_{RF}$ for 100 and 10,000 averages respectively. Note that this factor of 10 reduction in noise is predicted by the Dicke radiometer equation Eq. 2.15 for a factor of 100 times more averaging, as is shown in the red and green curves. Noise represents a 300 K antenna into a 100 K LNA for a total system temperature of 400 K. Signal is in a single bin at 200 MHz with a delta function line shape, defined in Eq. 2.19. The red, blue and green spectra represent 100, 1,000 and 10,000 averages respectively.

510 2.2.1 Signal significance

511 The problem of the extraction of signal from noise is fundamentally a statistical one since
 512 in general both the signal and noise are random variables. A method for computing a

513 *significance threshold* (ST) must be established, such that any bin containing more power
514 than this threshold is X % significant. In this way, it is possible have some known confidence
515 a given signal was not just a random fluctuation.

516 The probability that all N bins are less than z standard deviations $z\sigma$ for a standard
517 Gaussian distribution is given by

$$P(\max < z\sigma) = \left\{ \frac{1}{2} \left[1 + \operatorname{erf} \left(\frac{z}{\sqrt{2}} \right) \right] \right\}^N, \quad (2.33)$$

518 where P is the probability, $\operatorname{erf}(z)$ is the standard error function and z is real. Setting this
519 equal to 100%–X (where X is the *significance* or the desired probability a fluctuation crosses
520 the $z\sigma$ threshold assuming no signal), and inverting $\operatorname{erf}(z)$ yields a significance threshold
521 (ST). A convenient significance which was used in [add reference: levine et al](#) is X = 5%
522 corresponding to a 5% probability that an observed fluctuation above this ST is due to
523 chance rather than a significant effect (i.e. a signal). A 5% ST for $2^{10}/2 = 512$ frequency
524 bins works out to 3.9σ ⁹.

525 It should be noted that it is common in physics to discuss “ 5σ significance”. This means
526 that a given experiment has a $1 - \operatorname{erf}(5/\sqrt{2})$ probability (about 1 in 3×10^6) of a false positive.
527 The analysis of these normal spectra involves testing many independent frequency bins to see
528 if any one of them exceeds some threshold. It is helpful to view these bins as “independent
529 experiments”, each involving a random draw from the same parent Gaussian distribution.
530 In this context, we discuss global significance (all of the bins) in contrast to local significance

⁹Note that a real FFT produces half the number of frequency bins as an output compared to the time domain sample it received, hence the factor of 2

531 (a single bin). Setting a global 5% significance threshold is equivalent to setting a local
532 threshold of 3.9σ given 512 bins.

533 One point worth mentioning as it relates to the significance which is chosen is that of the
534 so called *cost* of a decision. If an experiment requires a facility which charges by the hour
535 and where the schedule is set years in advance, a false positive is quite expensive since it
536 will lead to publicity and ultimately humiliation. A follow up experiment will have to take
537 out more expensive time to verify the results, and until that happens theorists will spend
538 their time rewriting physics to explain the result. A similar line of logic holds for a false
539 negative, but that will be discussed later in Sec. [add reference: derive statistical power, prob](#)
540 [in analysis chapter](#). In this case, the global significance should be quite low to avoid this.

541 In the case of the dark radio experiment, a false positive is quite inexpensive. If a signal
542 is detected, just repeat the experiment. For run 1A, this is 9 days of averaging which is
543 mostly passive and is little more than an annoyance. If a signal is detected at the same
544 frequency, things become interesting. This concept of cost is discussed formally in Appendix
545 1 of Extraction of Signals From Noise by Wainstein and Zubakov [19].

546 For this reason, a significance of 5 % (i.e. 5 % chance of a false positive) is acceptable
547 for this experiment, where it is certainly not acceptable for other experiments.

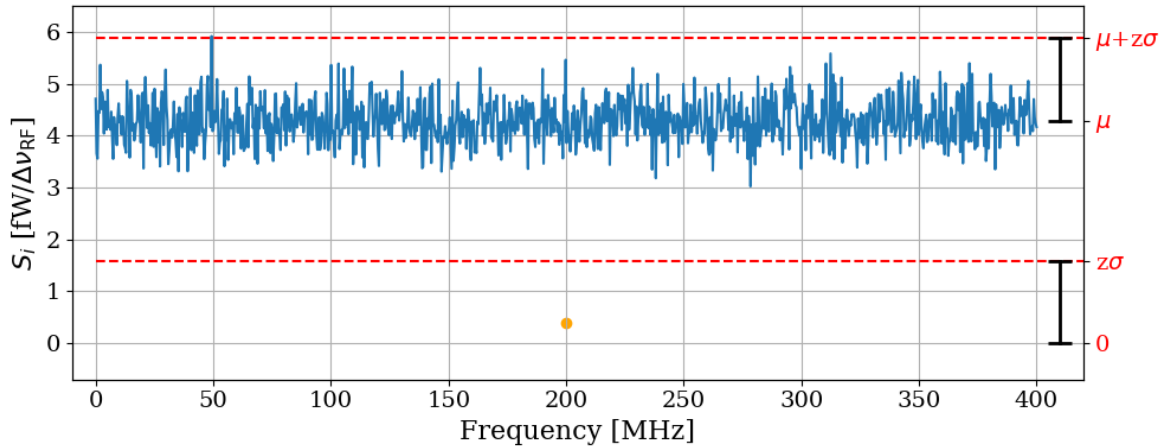


Figure 2.10: Simulated, input-referred noise spectrum containing small signal at 200MHz. The signal power = .4 fW, system temperature = 400 K and $N_{avg} = 100$; the same as is shown in the red spectrum of Fig. 2.9. The 0.4 fW signal is shown as an orange point. This power is added to the random background, so the measured power in the bin at 200 MHz is a Gaussian random variable given by Eq. 2.32. The significance threshold (upper dashed red line) is given by $\mu + z\sigma$ and was derived in section 2.2.1. The detection threshold (lower dashed red line) is the significance threshold minus the mean, $(\mu + z\sigma) - \mu = z\sigma$. This shows that the detection threshold is set by fluctuations of the measured power. While this is related to the ST, it is different. The detection threshold is below the mean, thanks to averaging. Note the detection at approxamately 50 MHz; this a random fluctuation and is expected to occur in 5 out of 100 simulations of these spectra since the significance used to calculate the ST was set at 5%. **comment: make detection thresh 'lime'**

548 **2.2.1.1 AASDFASDFS**

549 **2.2.1.2 Computing an exclusion limit**

550 With the significance threshold (ST) defined in for a spectra containing a signal in the
 551 previous subsection, we turn briefly to the concept of an exclusion limit. In the actual
 552 experiment, no signals were detected. In this case, the null result must be translated into
 553 an exclusion limit. While this section on toy analysis looks at small signals riding on noise

Number of Averages	True Positive [%]	False Negative [%]	False Positive [%]	True Negative [%]
100	0.2	99.8	5.7	94.3
971	16.3	83.7	5.5	94.5
1,760	49.8	50.2	5.7	94.3
2,782	83.8	16.2	5.7	94.3
10,000	100.0	0.0	5.6	94.4

Table 2.1: Caption

554 spectra, it can be easy to loose site of the fact that no signal was observed.

555 This experiment has one of two goals One common point of confusion can be cleared up

556 with an example. The significance thresh thinking that the significance threshold [W] sets

557 the limit above which one is 95 % confident

558 Really the limit is the threshold - the mean μ . This is usually significantly below the

559 significance threshold. This is demonstrated in figures asdfasdf

560 With the derivation of the significance threshold complete, the next subsection will focus

561 on predicting the amount of time.

562 2.2.2 Predicted time to detection

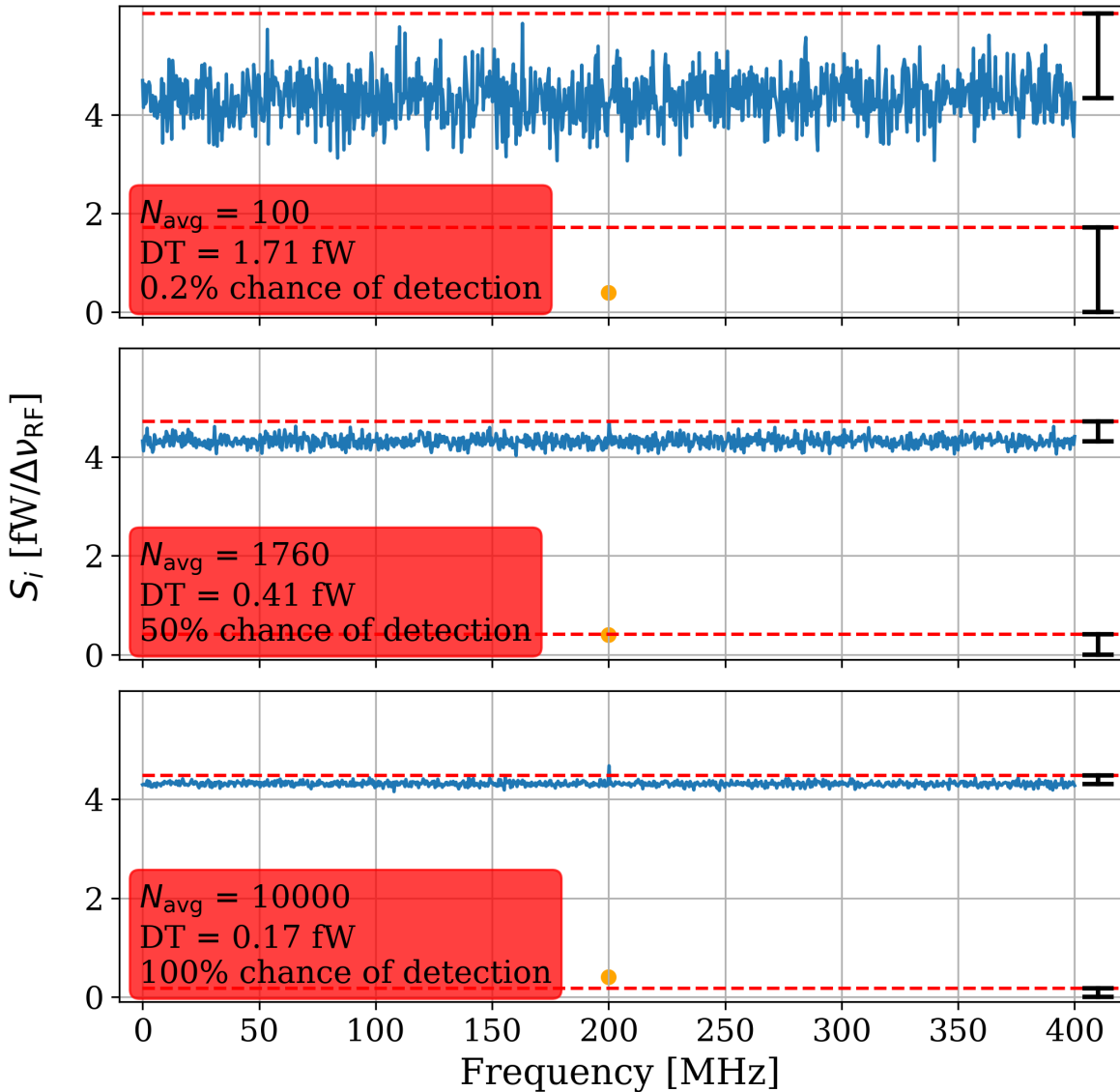


Figure 2.11: Simulated, input-referred noise spectrum containing small signal at 200MHz. The signal power = .4 fW, system temperature = 400 K and N_{avg} = 100, 1,760 and 10,000; the first and last are shown as the red and green spectra respectively in Fig. 2.9. The 0.4 fW signal is shown as an orange point. the chance of detection is computed via a simple Montie Carlo where 100,000 of similar spectra containing noise and signal are generated, and the number of times the measured power at 200 MHz is greater than the ST is counted. The full set of statistics from this Montie Carlo is shown in Table 2.1. **comment: make detection thresh 'lime'**

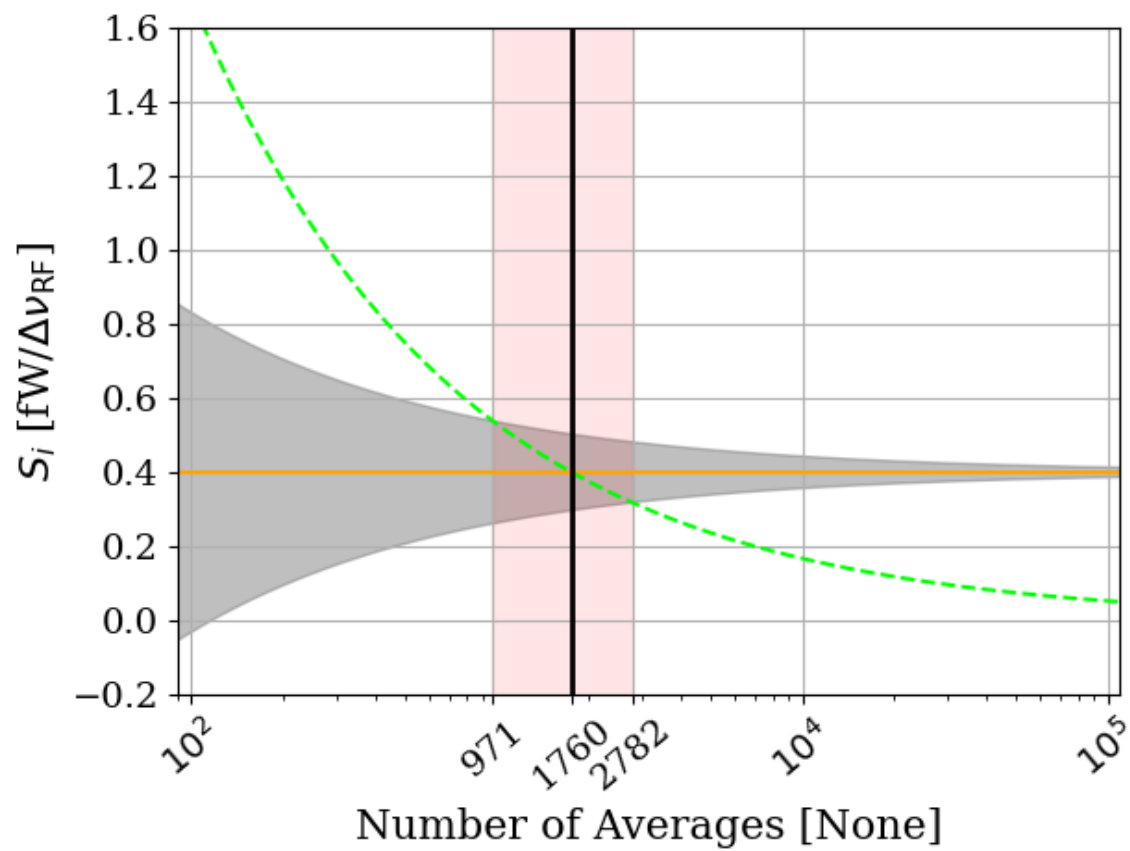


Figure 2.12: XXXX

563 **2.3 Thermal Noise in A Cavity**

564 **2.4 Reverberation Chambers and Statistical**

565 **Uniformity**

566 Generally it is convenient to thing of electromagnetic cavities as containing a single mode

567 **2.5 System Design**

568 This section outlines the subsystems which make up the experiment. While specifics and

569 basic calculations are provided as they apply to design choices of subsystems, testing and

570 characterisation of the system as a whole is covered in Ch. 3 and calibration of the system

571 is discussed in Ch. 4.

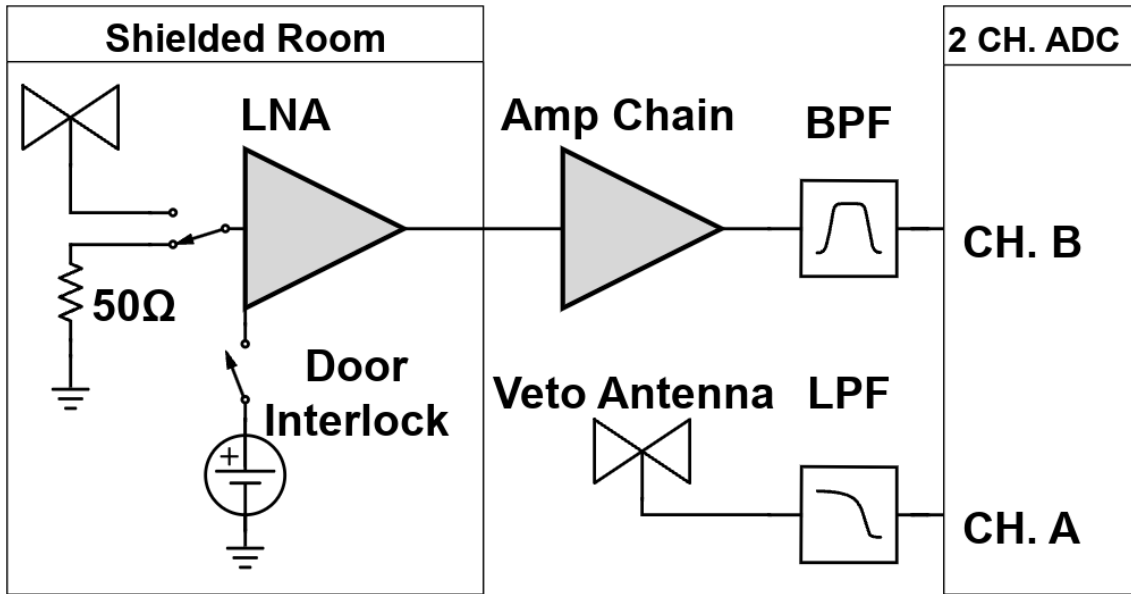


Figure 2.13: Schematic of the RF receiver system. An RF coax switch allows the PC to control the source (antenna or terminator). The switch is controlled by optical fiber to maintain isolation of the room. The LNA (Pasternack PE15A1012) has a nominal gain and noise temperature of 40dB and 100K (Figs. XXX and XXX). It is interlocked (Fig. 2.21) to the door to protect amp B and the ADC from large signals when the door is open. The secondary amplifier is a miniCircuits (MC) ZKL-1R5+ and has a nominal gain of 38dB. Not pictured after this amplifier is a fixed 4dB of attenuation. The band pass filter (BPF) is made up of a MC SLP-50+ high pass filter (HPF) and a MC ZX75LP-288-S+ low pass filter. The HPF reduces the bandwidth and therefore the total power of the signal before entering the ADC allowing for more gain before clipping. The LPF serves the same purpose while also acting as an anti-aliasing filter. These two filters define the experiment's bandwidth, $-3 \text{ dB} \approx 40 - 320 \text{ MHz}$. The veto antenna is outside of the room and interference is not reduced by the $\approx 100 \text{ dB}$ SE of the room, so no gain is required. The LPF on the veto is for anti-aliasing.

⁵⁷² 2.5.1 Shielded room

⁵⁷³ The shielding room [20] serves two purposes. The first is straightforward; to shield the
⁵⁷⁴ antenna, keeping radio frequency interference (RFI) *out*. The second purpose is a bit more
⁵⁷⁵ subtle; to keep any converted dark photons *in*. This second point is addressed further as an

576 aspect of system calibration in Ch. 4, but roughly can be described by the loaded quality
577 factor [21–23] of the antenna/room system. Namely, a more resonant system will be more
578 sensitive to coherent signals. This subsection will focus on the first point, keeping RFI out.

579 Shielding effectiveness SE is a measurement of a shielding enclosure’s ability to attenuate
580 electromagnetic waves from entering,

$$SE \equiv 10 \log_{10} \left(\frac{P_{\text{open}}}{P_{\text{closed}}} \right) = P_{\text{open}, dB} - P_{\text{closed}, dB} \quad (2.34)$$

581 where $P_{\text{open}}/P_{\text{closed}}$ are powers received with the door open/closed. The ratio of powers allows
582 all the specifics of antenna matching to cancel allowing for a very simple measurement.

583 Due to reciprocity between antennas, this is equivalent to measuring the attenuation
584 of waves leaving. The latter method is simpler and was performed. The IEEE standard
585 prescribing a very detailed SE measurement procedure [24] was used as a rough guideline
586 but the simple results presented here should be viewed as an estimate.

587 The SE was measured by placing a Rigol DSG-830 signal generator inside the room,
588 powered by the filtered 12 VAC Edison outlets inside the room. An antenna (bicon or
589 Vivaldi) was connected to the signal generator. Outside of the room, an identical antenna
590 (again, bicon or Vivaldi) was connected to a Rigol RSA-5065-TG spectrum analyzer. The
591 spectrum is scanned to find a frequency without local interference which would confuse the
592 results. The spectrum analyzer was set to attenuate its input to prevent clipping ¹⁰, and
593 the signal generator was set to output a sine wave at maximum power. The power measured

¹⁰The spectrum analyzer automatically calibrates the displayed spectrum to its internal attenuator and pre-amplifier. If external gain/attenuation are used, they must be accounted for manually.

594 on the spectrum analyzer is P_{open} of Eq. 2.34. The door was closed, attenuation removed
595 and P_{closed} was measured. In some cases the SE was so high a signal was buried below the
596 noise floor of the spectrum analyzer. These data are shown in red in Figs. 2.16 2.17.

597 SE can drop off to less than 80dB if the RF gasket around the door is not clean. Previous
598 day-long test runs detected several hundred signals which originated from RFI emitted from
599 the PC and several local radio stations. Cleaning was performed by scrubbing the copper
600 gasket and steel mating surface with red scotch-brite using denatured alcohol as a lubricant.
601 After two passes of polishing were complete, a layer of Deoxit D100L liquid was added.
602 Maintenance cleanings were performed using only Deoxit D5 spray. These signals were not
603 detected after the gasket was cleaned, which is consistent with calculations of Sec. XXX

604 The primary RFI in the 50-300 MHz span are from local radio broadcasts. The strongest
605 of this is around $100 \mu\text{V}/\text{m}$ as measured in the lab. There are also many lower level peaks
606 which span the entire frequency range, though are more pronounced in a few frequency bands
607 (60-75MHz, 130-140Mhz, 270-290MHz). These peaks come from the PC which serves at the
608 spectrum analyzer. Before the door was cleaned, many of these signals were detectable, but
609 cleaning the door resulted in a clean spectrum for the 9 day data run. The spectrum from
610 the veto antenna (discussed in Sec. XXX) is shown in Fig. 2.14

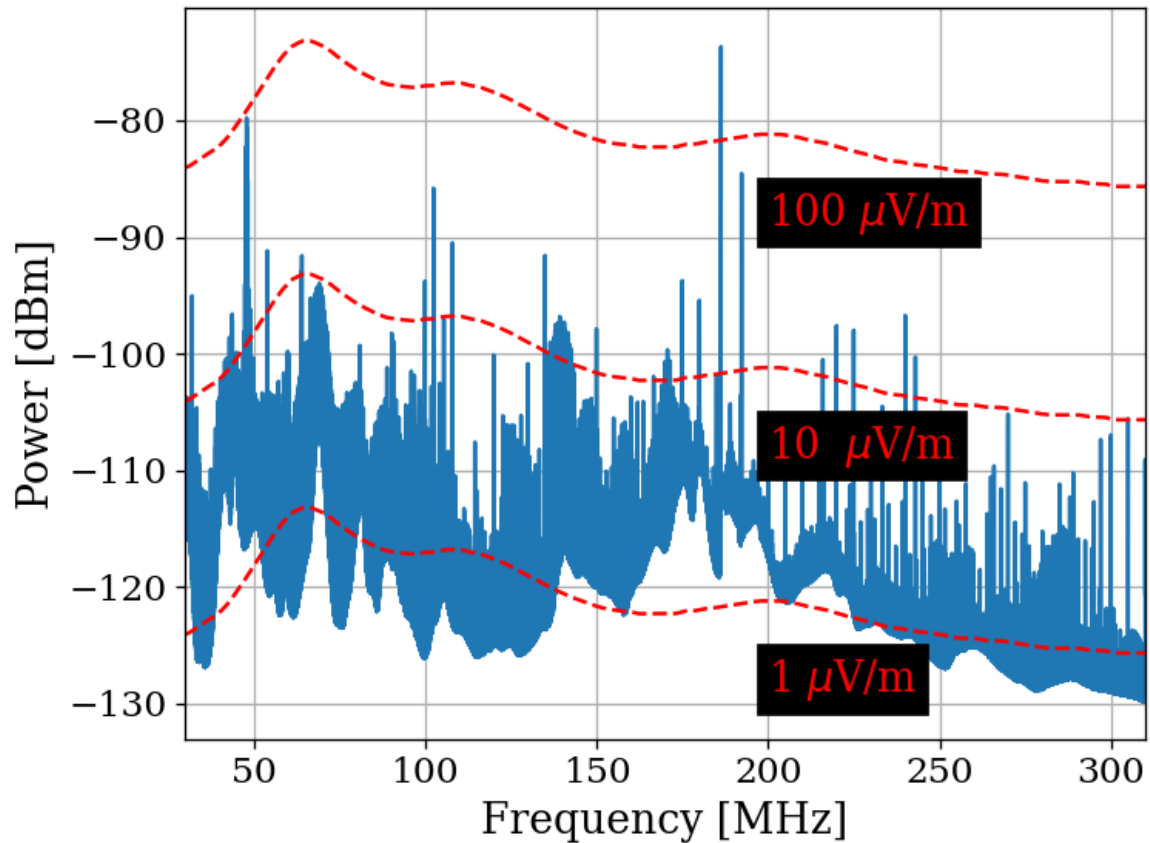


Figure 2.14: Spectrum from veto antenna during 300MHz data run. Spectrum plotted as measured power in dBm. Red curves indicate the equivalent field strength. The curves track the antenna factor with frequency for the COMPOWER AB900 [25] bicon. Two identical AB900 antennas are used, one to search for dark photons in the shielded room, and a second to monitor the local RFI background.



Figure 2.15: Photo showing set up to measure SE of 314. Photo taken using Vivaldi antennas for data shown in Fig. 2.17. The same set up was used with bicon antennas for the 50-300 MHz data shown in Fig. 2.16. Bicon antenna shown in background of photo was not in use for this test.

314 Shielding Effectiveness

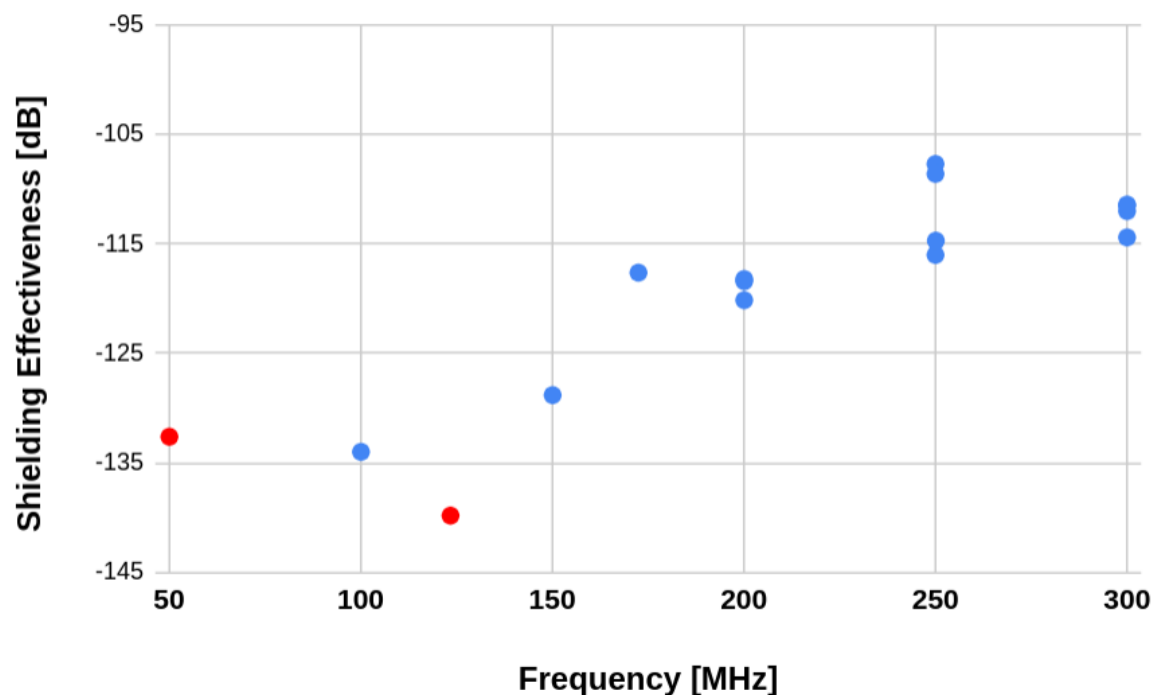


Figure 2.16: Shielding effectiveness of shielded room measured with Bicon antenna. Red points indicate measurements limited by the noise floor of the spectrum analyzer located outside and are an upper limit; true SE is lower (better). Measurement would require a stronger amplifier inside the room. At a few frequencies the antenna inside the room was moved to get a sense of the uncertainty of the measurement.

314 Shielding Effectiveness

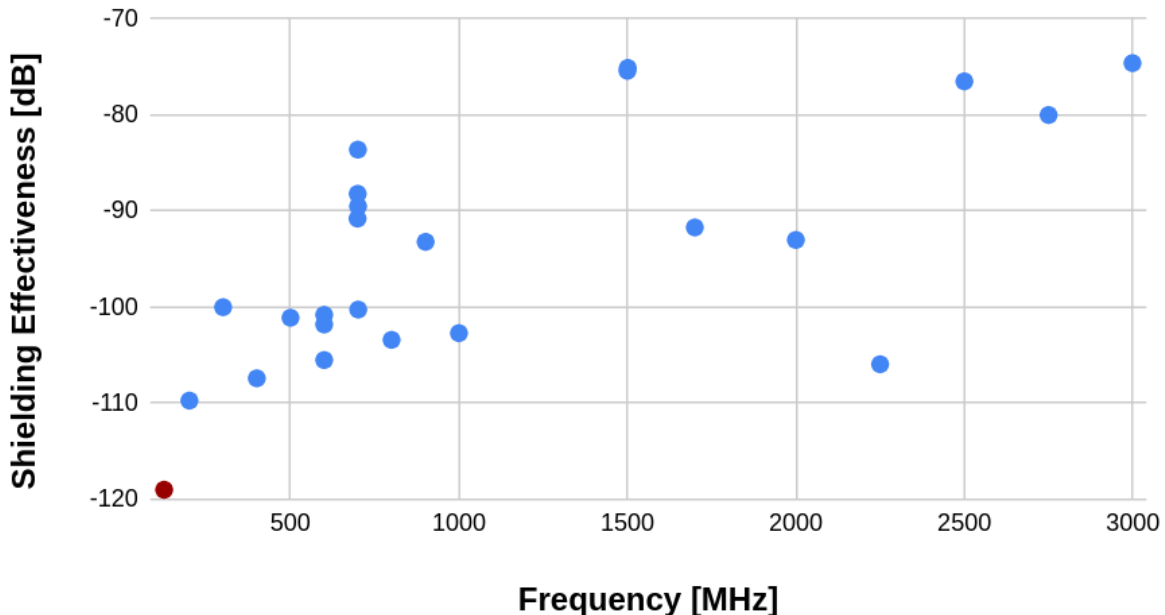


Figure 2.17: Shielding effectiveness of shielded room measured with Vivaldi antenna. Red points indicate measurements limited by the noise floor of the spectrum analyzer located outside and are an upper limit; true SE is lower (better). Measurement would require a stronger amplifier inside the room. At a few frequencies the antenna inside the room was moved to get a sense of the uncertainty of the measurement.

611 **2.5.2 Antenna**

612 The antenna plays an important roll in the experiment as the matching device between elec-
613 tromagnetic waves in the cavity and the receiver system. For a broadband search such as the
614 50-300 MHz run (a 6:1 bandwidth), a broadband antenna must be used. The chosen antenna
615 must provide a good impedance match and high efficiency since an inefficient antenna would
616 convert a substantial amount of the converted dark photon's power into heat in the antenna's
617 structure. For the 50-300 MHz run, a ≈ 131 cm biconical antenna (bicon) was chosen. The
618 selected model is manufactured by COMPOWER, model AB-900A [25]. In a phone call with
619 the manufacturer as well as testing of the isolated balon, it was determined that the balun
620 used in the antenna was 1:1. This allows for simple simulation. In COMSOL, the lumped
621 port option allows for a balanced drive of an antenna. A match to a 50Ω transmission line
622 through a 1:1 balun is simply modeled as a lumped port, a very simple object in COMSOL
623 featured in nearly all of the antenna tutorials ¹¹

¹¹See for example the dipole antenna tutorial, available at <https://www.comsol.com/model/dipole-antenna-8715>

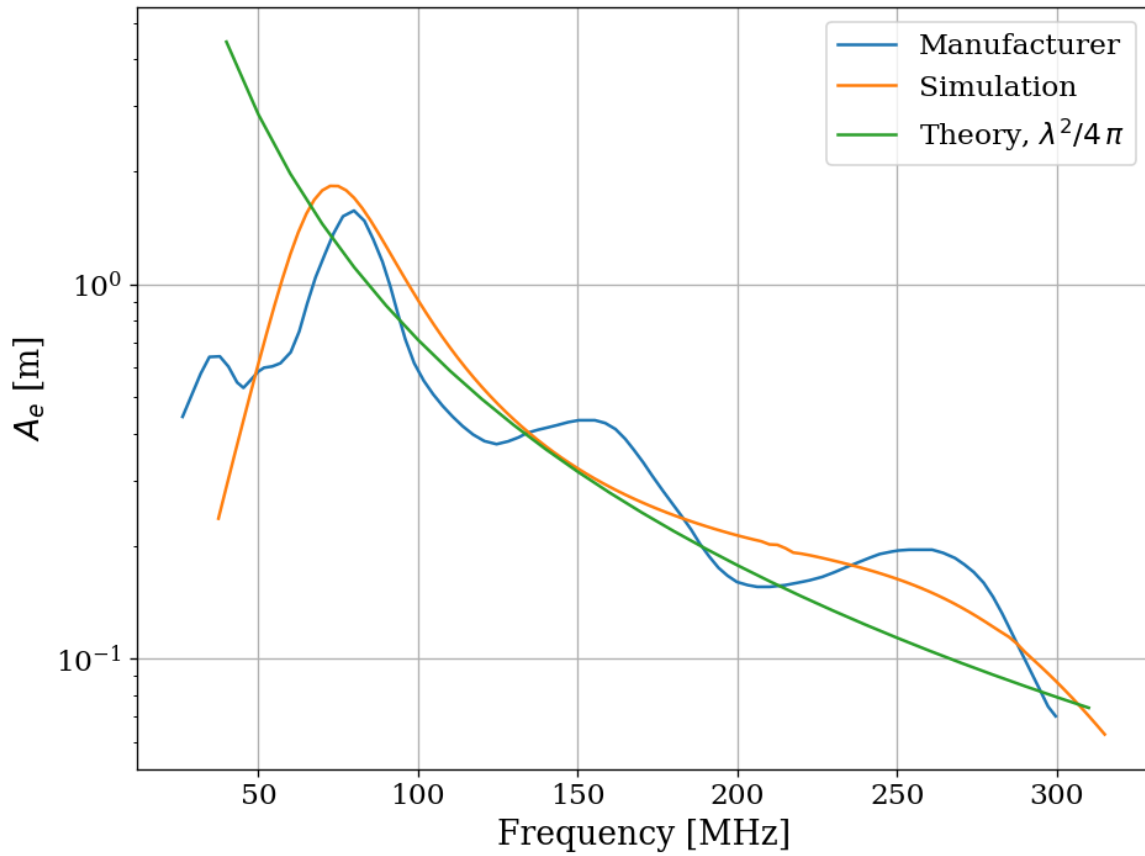


Figure 2.18: AB-900A biconical antenna effective aperture, simulated, measured and theoretical in free space. Simulation performed in COMSOL. The measurement was provided by manufacture [25] as an antenna factor and was converted using Eq. xxxx.

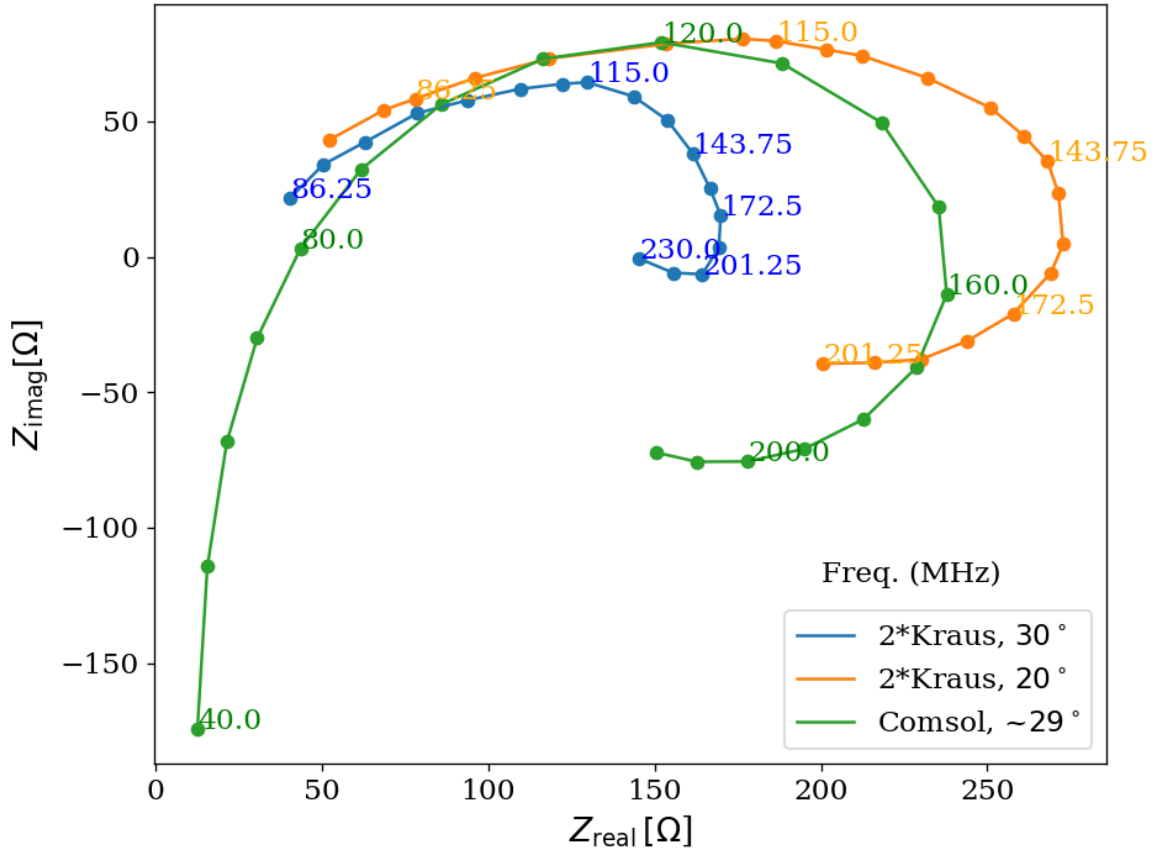


Figure 2.19: Simulated AB-900A biconical antenna free space complex input impedance shown in blue. Simulation was performed in COMSOL. Measurement from Kraus, second edition, Fig 8-13 [26], reproduced here in Fig. 2.20. Measured data is for a monoconical antenna and must be multiplied by 2 to compare to a biconical antenna. Numbers along curve indicate frequency in MHz.

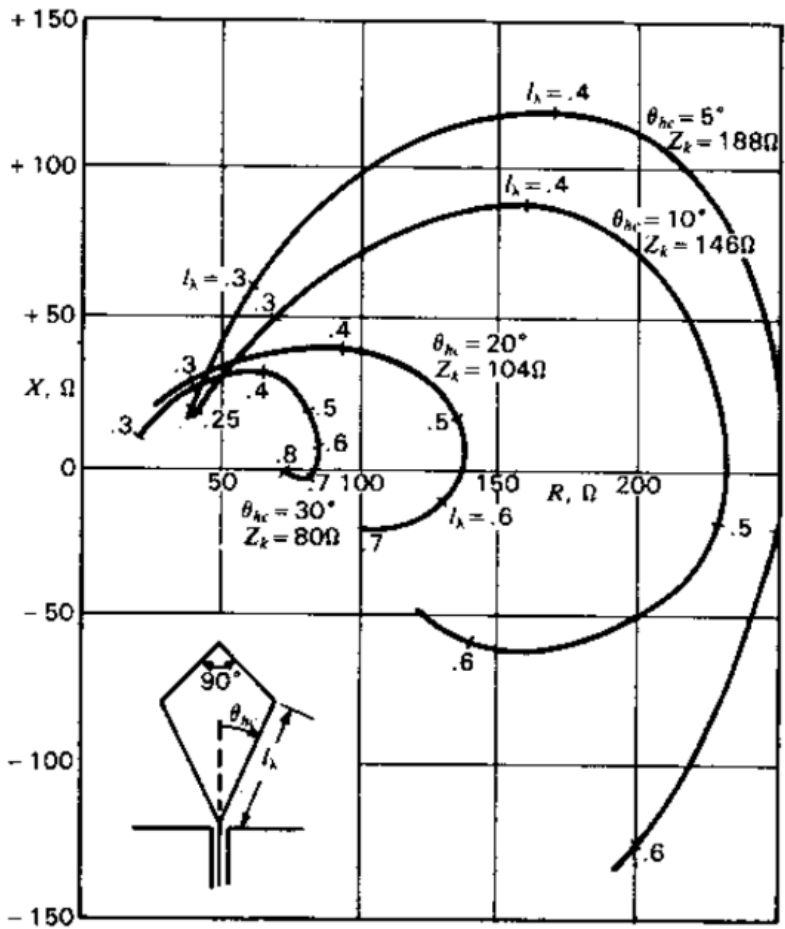


Figure 8-13 Measured input impedance of single cones with top hat as a function of cone length in wavelengths (l_λ). Impedance curves are presented for cones with half-angles of 5, 10, 20 and 30°.

Figure 2.20

624 **2.5.3 Terminator and fiber-optic switch control**

625 Experience has shown that it is advantageous to have a stable noise reference at the beginning
626 of the signal chain to measure periodically to monitor system function. One may think the
627 antenna can provide this following Sec. 2.3. In practice, it measures slightly less than this,
628 and has some frequency dependant variations. Furthermore, while RFI was not significant in
629 the actual run, it very well could have been, introducing some uncontrolled, coherent, power
630 into the spectrum which would have had an unknown origin. A terminator will give a very
631 constant $S_{\text{term}} = kT$ regardless of RFI and antenna position. For this reason one is included.
632 It is at the same temperature as the walls, and is a nice passive solution. The RF switch
633 shown in Fig. 2.13 is actuated periodically during the run to measure the terminator's noise
634 power. The switch is controlled via a fiber optic link in order to reduce RFI. The fiber optic
635 is an extremely important feature which was overlooked for several years at the beginning
636 of the experiment leading to lots of RFI.

637 **2.5.4 Low noise amplifier**

638 The important concepts of the LNA have been introduced in Sec. 2.1.4. Relevant specifica-
639 tions for the Pasternack PE15A1012 [16] are summarized in table 2.2.

640 We have several identical amplifier which are labeled with letters. At the time of writing,
641 amplifiers A-D are out of commission. Amplifier E was used for run 1.4.

Specification	Value	Uncertainty (50-300MHz)	Units
Frequency Range	50-1,000	-	MHz
Gain	40	± 1	dB
Noise Temperature	110	± 10	K
Input Return Loss	< 15	-	dB
Output Return Loss	< 15	-	dB
Price	500	-	USD
Voltage	9-15		V

Table 2.2: Specifications for the Pasternack PE15A1012-E. The voltage is regulated internally, so the exact voltage supplied is not critical

642 2.5.5 Signal conditioning

643 comment: left off in here 7/10

644 As discussed in Sec. 2.1.5, the ADC has internal signals. To mitigate them, external
 645 gain should be added to the signal. This gain must be carefully however since too much will
 646 cause the ADC to clip. To accomplish, several RF components must be selected to condition
 647 the analog signal: a secondary amplifier, band pass filter and and several attenuators.

648 As discussed in 2.1.4, the noise temperature of a secondary amplifier has negligible impact
 649 on the total system noise temperature. For this reason a cheaper secondary amplifier is used.
 650 The specifications for the miniCircuits ZKL-1R5+ [27] are outlined in Table 2.3.

651 The total gain required can be estimated by setting the output referred power of bandlim-
 652 ited 400 K noise source times the gain equal to the maximum power the ADC can handle,
 653 $V_{\text{RMS}}^2/Z = 0.63 \text{ mW}$. Assuming a perfect filter from 50-300MHz the gain required is

$$G = \frac{0.63 \text{ mW}}{k 400 \text{ K} 250 \text{ MHz}} = 4.5 \times 10^8 = 87 \text{ dB.} \quad (2.35)$$

Specification	Value	Uncertainty (50-300MHz)	Units
Frequency Range	50-1,000	-	MHz
Gain			
Noise Temperature			K
Input Return Loss	<	-	dB
Output Return Loss	<	-	dB
Price		-	USD
Voltage	9-15		V

Table 2.3: Specifications for the miniCircuits ZKL-1R5+. The voltage is regulated internally, so the exact voltage supplied is not critical

654 Noise is a random process however. This much gain would mean that plus/minus 1σ of
 655 the time domain samples are below clipping. Since many are collected ($2^{24} \approx 1.6 \times 10^7$ in
 656 run 1.4), many samples will clip with this much gain. However, it gives a good estimation
 657 for what to expect.

658 Setting the gain requires a secondary amplifier must be chosen. Next, a band-pass filter
 659 is chosen with good pass band be

660 Experience and preliminary simulations have shown that a few dB of clipping for an
 661 extremely noisy signal actually doesn't matter much, but this was not fully explored since.

662 **2.5.6 Veto antenna**

663 **2.5.7 12 V power system**

664 Slow turn on circuit

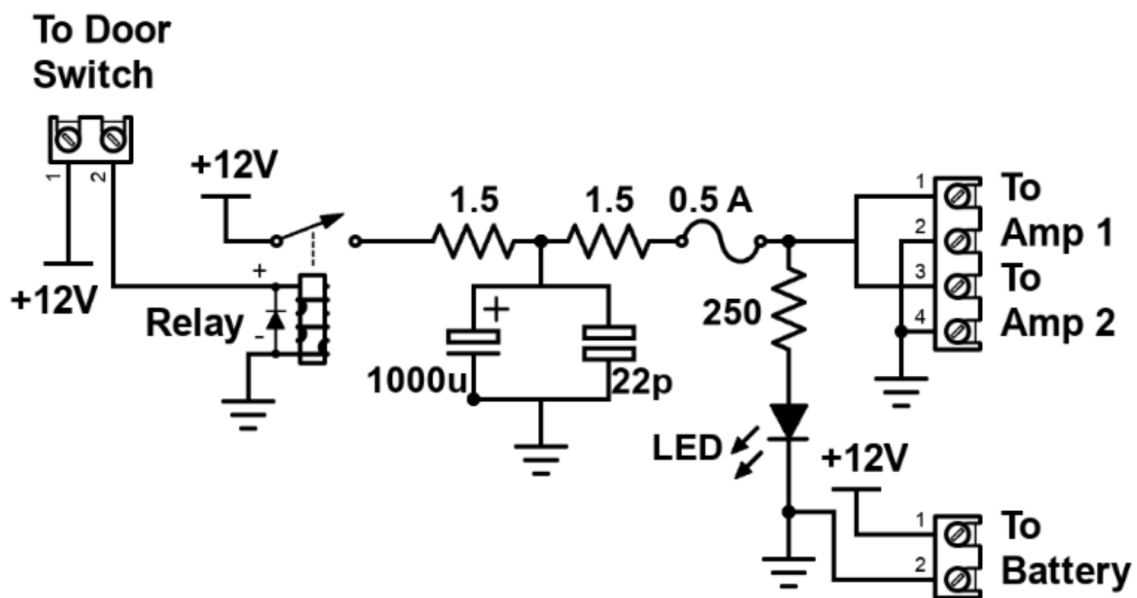


Figure 2.21: Schematic of Interlock board. No voltage regulation is provided because it is designed to work with amplifiers containing internal regulation (Pasternack PE15A1012). Not shown is a simple "slow turn on circuit" consisting of a 0.68 F capacitor and a 8Ω , 10 W resistor (time constant = 5.4 seconds) which was installed to protect the amplifier from transient voltages when the door is closed. Experience has shown the liberal use of fuses to be prudent when working with car batteries in a metal room.

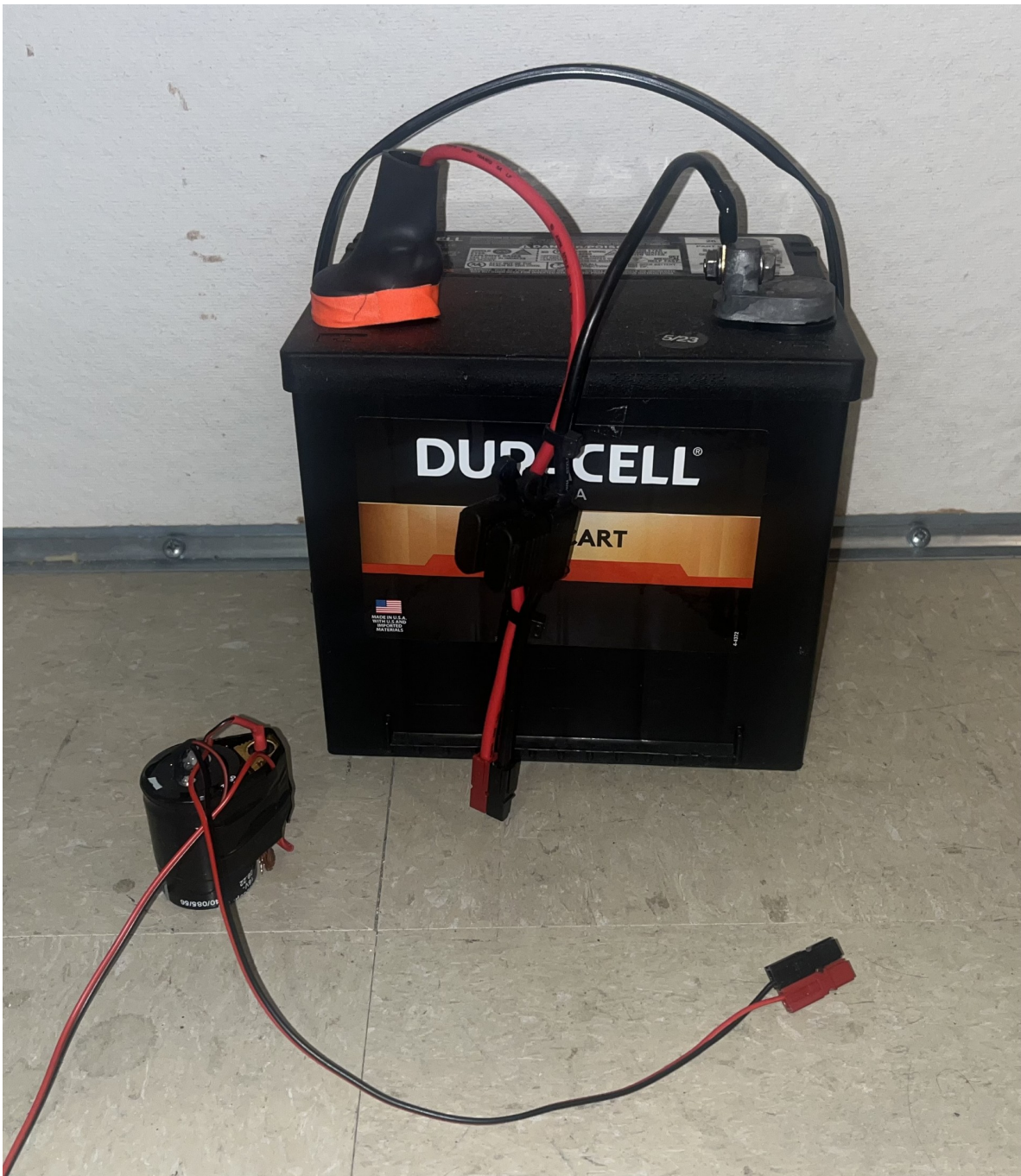


Figure 2.22: Photo of 12V lead-acid battery and slow turn on circuit. Both connect directly to the interlock board shown in Fig. 2.21. Slow turn on circuit is connected between interlock board and amplifier. Battery includes a 2A fast fuse installed in commercial Anderson power pole assembly.

665 **2.5.8 GPU-Based Real-Time Spectrum Analyzer**

666 The use of commercial Spectrum Analyzers (SAs) which feature so called RTSA (real time
667 spectrum analyzer) mode come with several restrictions which limit the efficiency with which
668 they are able to perform wide-band scans with narrow frequency resolution as we point out
669 in our pilot run [GroupPaper]. The number of frequency bins output by an discrete Fourier
670 transform (DFT) is equal to the number of time domain samples/2, while the bandwidth
671 is given by sample rate/2. Furthermore, the ability to acquire data in real time requires a
672 DFT algorithm (generally implemented as a fast Fourier transform, FFT) and computation
673 resources which can operate on time domain data at least as fast as it is acquired. From
674 a practical perspective this means that high frequency resolution, wide bandwidth, real
675 time DFTs require modest memory, transfer rates and processing resources. By employing
676 frequency mixers, restrictions on bin counts, and dead time between acquisitions, commercial
677 SAs are able to reduce hardware demands. For this reason we have constructed our own
678 SA based on the Teledyne ADQ32 PCIE digitizer. As a point of reference, the system used
679 in this data run has the specifications outlined in table 2.4. While modest by modern PC
680 standards, these specifications are generally not implemented in commercial SAs.

Bit depth	16 bits
Sample rate	800MHz
DFT input length	2^{24} samples
FFT compute time	2 ms
Channel count	2

Table 2.4: Specifications for the spectrum analyzer used for run 1A.

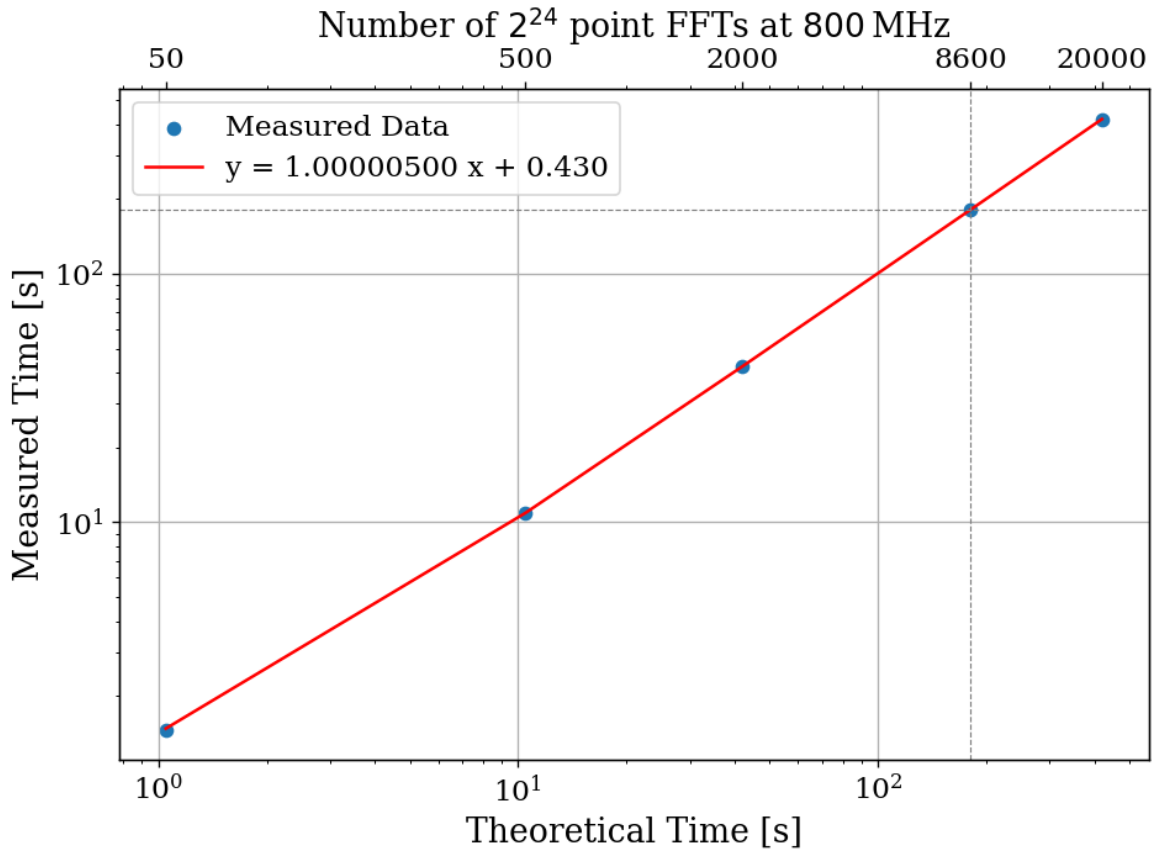


Figure 2.23: Acquisition efficiency for GPU-based Real-time spectrum analyze computed from measured vs theoretical times. The constant offset of 0.43 seconds corresponds to a small set up period when starting an acquisition containing, in the case of run 1A, 8600 FFTs. In the limit of an infinite length acquisition, the system's efficiency can be read off from the slope and is 99.9995%. The more realistic efficiency is a function of number of FFTs per acquisition and for run 1A = $180.3551 \text{ [s]} / 180.7782 \text{ [s]} = 99.765\%$.

681 2.5.9 Spectrum Analyzer Details

682 After passing through and amplifier and filter chain outlined in section ??, both the main and
 683 external antenna signals are digitized by the ADQ32's two ADCs. We utilize a GPU direct
 684 write in order to minimize CPU-GPU copies which in our experience tend to be significantly
 685 slower than the FFT itself. This GPU direct write is implemented by the digitizer's C++

686 API. First, several buffers are allocated in GPU memory.

687 Once written to a pre-allocated, time-domain buffer in the GPU's memory, an FFT is
688 performed using Pytorch which we found to be the fastest across all the GPUs we tested (all
689 Nvidia). [28]

⁶⁹⁰ **Chapter 3**

⁶⁹¹ **System Characterization and Data**

⁶⁹² **Acquisition**

“When you can measure what
you are speaking about and
express it in numbers you know
something about it; but when
you cannot measure it, when
you cannot express it in
numbers your knowledge is of
meagre and unsatisfactory kind;
it may be the beginning of
knowledge but you have
scarcely progressed in your
thoughts to the stage of science
whatever the matter may be.”

- 694 • Schematic of experiment
- 695 • Detailed schematic of amp chain
- 696 • Reason for switching. Cite dickie thermal equilibrium of resistor and antenna in cavity
- 697 [29]. See 5.9.23 Messing around with different loads in lab book for experiment.
- 698 FROM PAPER 1A DRAFT: The dark E-field radio experiment consists of a biconical E-
- 699 field antenna inside of a cavity. The cavity is implemented as a room temperature commercial
- 700 shielded room (maufactured by ETS Lindgrin) which serves both to isolate the experiment
- 701 from external radio frequency interference (RFI) and to provide resonant enhancement of
- 702 any (coherent?) dark photons after they have converted to standard photons. A low noise
- 703 amplifier (LNA), secondary amplifier, attenuation and a band pass filter provide analog
- 704 signal conditioning before the signal is digitized by a GHz ADC (Teledyne ADQ-32), see
- 705 figure 2.13. From the digitizer, records of length 2^{24} are written to a GPU where a fast
- 706 Fourier transform (FFT) is performed. Approximately 8000 FFTs are performed and added
- 707 to a running total on the GPU (representing about 3 minutes of real time data) before
- 708 dividing by the number of FFTs and copying this averaged spectrum to RAM where it can
- 709 be saved for future processing, including further averaging. This pre-averaging reduces the
- 710 ≈ 3 GB/s/channel data stream from the ADC to the GPU down to ≈ 0.3 MB/s/channel
- 711 which allows for real time copies from the GPU to RAM but comes at the cost of temporal
- 712 resolution of transient candidates. This is summarized in Fig. 3.1.

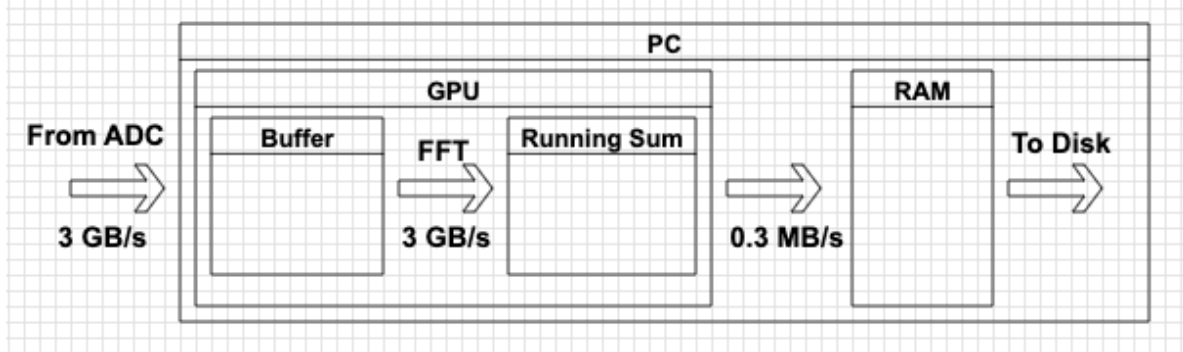


Figure 3.1: Data stream of real time DAQ. This set up is duplicated for channels A and B

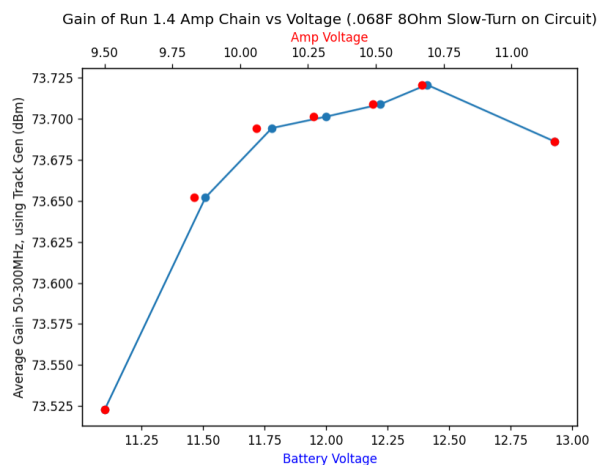
⁷¹³ 3.1 Control and Quantifying of Uncertainties

⁷¹⁴ 3.1.1 Direct Measurement of Amp Chain Parameters

⁷¹⁵ • Gain

⁷¹⁶ • Noise schematic

Figure 3.2: Gain vs. voltage of front end amplifier



717

ADD fig

⁷¹⁸ Chapter 4

⁷¹⁹ Data Analysis and Calibration

720 We will build up this search in two successive steps. First a basic analysis on the averaged
721 spectrum (roughly equivalent a *processed spectrum* in [haystac[•]2017]) which sets a relatively
722 simple, though conservative limit. The second step accounts for the variation of Q with
723 frequency. This comes into play because a dark photon line with Q = 1e6 would span a
724 single 50 Hz bin at 50 MHz but would span 6 bins at 300MHz. This is accomplished with
725 a signal-matched filter in the frequency domain to improve SNR by compressing the signal's
726 power into as few bins as possible. We observe a small improvement at 50MHz (where the
727 signal is expected to span only a bin or two) and a factor of XXXX improvement at 300MHz,
728 and a linear(JL: check this claim) improvement-factor between these two extremes.

729 Following an exploration of the details of the analysis pipeline, we take a step back and
730 place the analysis in a black box and perform a Monte Carlo validation of our sensitivity
731 by injecting signals onto a generated background. Our background is white noise riding
732 on a slowly varying undulations and is therefore simple to generate. We employ a simple
733 Monte Carlo method to find the XXXX% confidence limit on power which we would be able
734 to detect. In the absence of a signal, this limit on power can be converted into a limit on
735 epsilon.

736 4.1 Hardware Injection Test ¹

737 To validate detection methodology, a separate, proof-of-concept run with an a proxy dark
738 photon signal injected into the shielded room was performed. Apart from the injection

¹Code for this section can be found at: <https://github.com/josephmlev/darkRadio/tree/master/daqAnalysisAndExperiments/run1p4/injectionTesting/injectionTesting.ipynb>

739 antenna (a 40 cm monopole, see Sec. [add reference: simulation validation](#)), the setup was
740 equivalent to run 1.4, including the data analysis. The proxy dark photon signal (detailed
741 in Sec. 4.1.1.2) was injected at a frequency set by a colleague and was unknown to me at
742 the time of analysis, constituting a “blind” analysis.

743 4.1.1 Injection test prerequisites

744 4.1.1.1 Determination of required injected power

745 **comment:** S parameters need to be squared. Check on this. See Besnier [30] To accomplish
746 the test, a minimum detectable power required for injection P_{inject} must be computed. P_{inject}
747 should correspond to a signal that can be detected in a predictable amount of time (with some
748 uncertainty, discussed in detail in Sec. [add reference: plot of expected time to detection in](#)
749 [toy analysis](#)). A simple way to begin is to read off the detectable, total integrated, power from
750 Fig. [add reference: output referred limit from paper](#). In other words the power contained in
751 a dark photon line, integrated over the few bins spanned by the line ($Q_{\text{DP}} \approx 10^6$, discussed
752 in [add reference: discussion of dp Q, probably ch 1](#)) This gives the amount of output-referred
753 power that would be detectable 95% of the time after 9 days of integration. Since we don’t
754 want to wait 9 days for this test, it is simple to convert this detection limit into one which
755 would be produced in a shorter time by the Dicke radiometer equation, Eq. 2.15. Namely,
756 the limit on power scales like the square root of time ², so a one hour integration will require

²It is important to point out that one needs to test whether or not the system in question actually behaves as predicted by the Dicke equation for the amount of averaging in question. After lots of averaging, one may encounter non-thermal backgrounds which do not scale properly. It is shown in [add reference: ch 3 probably](#) that the dark radio system follows the Dicke radiometer equation at least for 9 days. It is also shown for this specific run in Figs. 4.5 and 4.6. **comment:** If you do a simulated spur run/RFI run you can

757 a factor $\sqrt{9 \text{ days}/1 \text{ hour}} = 14.7$ more power than is shown in [add reference: output referred](#)

758 limit from paper.

759 At this point the simplest way to proceed is to measure the average through power

760 of the monopole to the bicon in several antenna positions $\langle S_{21} \rangle$. This is the same as the set

761 up described in Sec. [add reference: simulation validation, and figure of CAD](#). The bicon was

762 moved to 9 positions and the resulting S parameters were measured at the reference planes

763 shown in Fig. 4.1. They are shown in Fig. 4.2 after being averaged together.

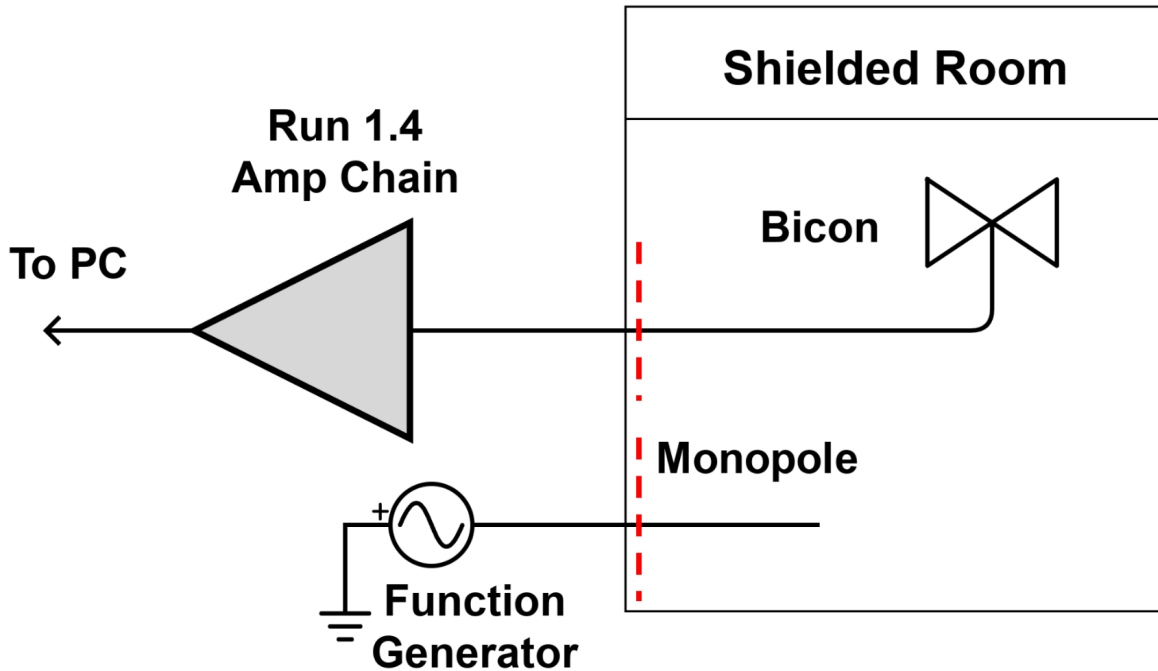


Figure 4.1: Schematic of hardware injection test. Dashed red lines indicate reference planes used to measure S parameters, shown in Fig. 4.2. “Amp Chain” includes everything shown in Fig. [add reference: amp chain schematic, prob ch 2](#)

show it's longer.

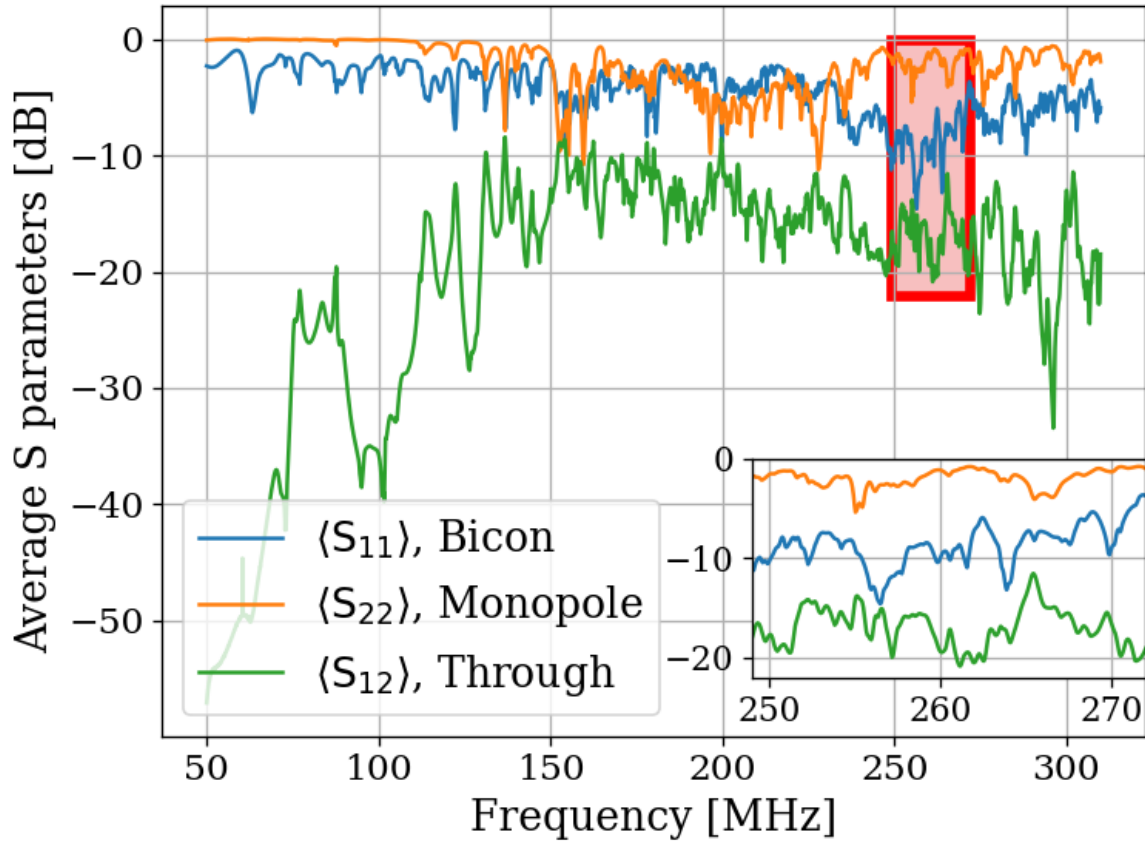


Figure 4.2: Average S parameters of hardware injection test. Taken at 9 positions of the bicon antenna and averaged together (linearly). Ports 1 and 2 are defined to be for the bicon and monopole respectively. Note that $\langle S_{12} \rangle = \langle S_{21} \rangle$ so only $\langle S_{12} \rangle$ is shown. Inset shows zoom on area enclosed by red box.

764 Knowing the output-referred limit, the system's average S_{21} , and the gain G, allows for
 765 a calculation of the required signal strength (as a function of frequency) which will become
 766 detectable after a known amount of time. In order to simplify the test, a smaller 1 MHz band
 767 is chosen between 268 and 269 MHz for the blind injection, where S_{12} is constant to about
 768 1dB. At first glance, this seems to be cheating, however there are still approximately 21,000
 769 frequency bins in this span, so a detection is very unlikely to be random. Furthermore, the

770 entire 50-300 MHz span is sent to the detection algorithm (Fig. [add reference: detection alg. from paper](#)) which produces an output without knowing about this frequency restriction.

With all this in mind, the signal power required is simply

$$P_{\text{inject}} = \frac{P_{\text{o}}^{\text{lim}}}{G \langle S_{21} \rangle},$$

772 where each term is a function of frequency. For the parameters described in this section
773 (including the increase in the power limit $\sqrt{9 \text{ days}/1 \text{ hour}} = 14.7$), this works out to \approx
774 $6 \times 10^{-19} \text{ W}$ or -152.5 dBm. The Rigol DSG830 signal generator is not calibrated to such
775 low levels, so this was achieved through attenuation ³.

776 4.1.1.2 Proxy dark photon signal injection

777 Now that the power for signal injection has been established, the finite-width proxy-signal
778 ($Q_{\text{DP}} \approx 10^6$) can be generated. An intuitive way to accomplish this would be with an
779 arbitrary waveform generator injecting a time domain signal which is the Fourier transform
780 of the the expected Rayleigh line shape, Eq. 2.23. This is the method of the ADMX
781 experiment (see for example [31]). Another option would be to frequency-modulate a sine
782 wave such that it slowly sweeps out the line shape, spending am amount of time at each
783 frequency weighted by Eq. 2.23. While intuitive, I was unable to get this to work. Zhu et
784 al.'s method of frequency hopping [32] is the discretized version of this and it very simple
785 to implement. The signal generator is set to change frequencies at some interval (discussed
786 below). The frequency which is set is randomly drawn from the PDF of Eq.2.23.

³Experience with this signal generator has shown it exhibits the best performance is when it is set around -30 dBm. Higher than this, large non-harmonic distortions appear contaminating the run. Smaller, and the signal-to-spurious-noise-floor of the generator is poor, also contaminating the run.

787 There are two considerations that determine the frequency hop period τ_{FH} that the
788 frequency is changed⁴. First, τ_{FH} should be much longer than the acquisition time of a
789 single buffer τ_{FFT} ⁵. On the Rigol signal generator, the power is briefly shut off while the
790 frequency is changed. $\tau_{\text{FFT}} \ll \tau_{\text{FH}}$ ensures that most FFTs of data which don't contain a
791 frequency-hop. Second, τ_{FH} should be small compared to the total time of integration τ , so
792 that there are many frequencies represented in the entire run. In the limiting case, $\tau_{\text{FH}} = \tau$
793 will yield an averaged spectrum containing a single injected frequency; the proxy-signal will
794 be a delta function in the frequency domain.

795 Testing has shown that $\tau_{\text{FH}}/\tau_{\text{FFT}} \approx 10$ is more than adequate to address the first consider-
796 ation. For run 1A (and therefore, this test which shares settings with run 1A), $\tau_{\text{FFT}} = 2^{24}/800$
797 MHz = 21 ms, so τ_{FH} was set to 250 ms. This means that over 1 hour, the frequency will be
798 set to $\approx 1.4 \times 10^4$, which addresses the second concern. A histogram of this signal is shown
799 in Fig. 4.3.

⁴Zhu et al. randomized this period to prevent any unintentional periodic signals entering. I didn't find this to be necessary.

⁵One can likely bypass this restriction by coordinating the signal generator and ADC such that there is some dead time between collection of buffers, in which the frequency is set. Testing has shown that this restriction is adequate to avoid this extra programming step

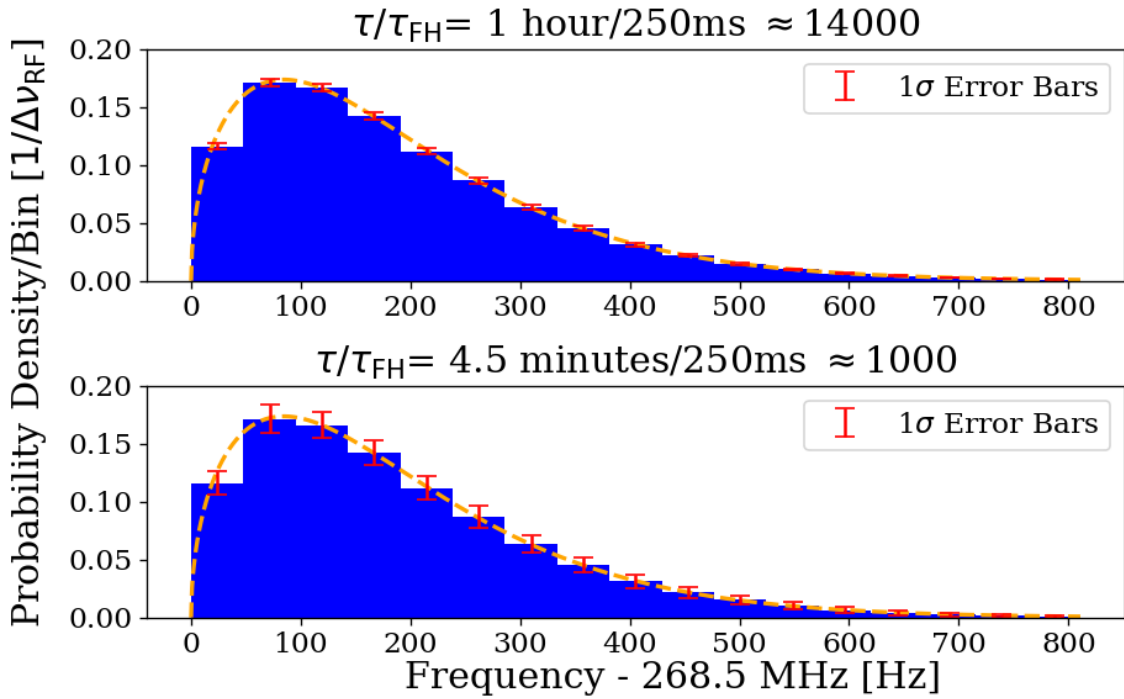


Figure 4.3: Histogram of frequencies used for hardware injection test, with realistic $\Delta\nu_{RF} = 47.7$ Hz. Orange dashed curve is expected line shape from 2.23. Blue histogram and error bars generated from Monte Carlo simulation and shows the mean value per bin, with 1σ error bars in red. This involves generating 1000 lists of random frequencies (each of length τ/τ_{FH}), binning the data and calculating the standard deviation of each bin. τ is the total acquisition time and τ_{FH} is the amount of time spent on each frequency before “hopping” to the next. Their ratio, τ/τ_{FH} is the number of frequencies which are injected in a given injection test, and was approximately 1.4×10^4 for the one hour test outlined in this section.

4.1.2 Performing the injection test

Due to the uncertainties involved, more data were taken than the required 1 hour. This also helped produce the pretty plot in Fig. 4 of Levine et al. [add reference: levine et al.. 3.6](#) hours of data were collected, and saved in 30 second pre-averages so that progressively more data could be averaged if the signal was not detected at the predicated time. As mentioned

805 above, the signal injected was at high frequency so that it would be split up into 5 or 6
806 bins, testing the matched filter's effectiveness. The bicon was moved to 9 positions. Spectra
807 resulting from 9 antenna positions and 30 seconds of pre-averaging at each position were
808 averaged together giving 4.5 minute time resolution. Three of these spectra are shown in
809 Fig. 4.4. The standard deviation of these spectra average down with the square root of
810 time, closely following the Dicke radiometer equation (discussed in Sec. [add reference: ch](#)
811 [2?](#)). This is shown in Figs. 4.5 and 4.6.

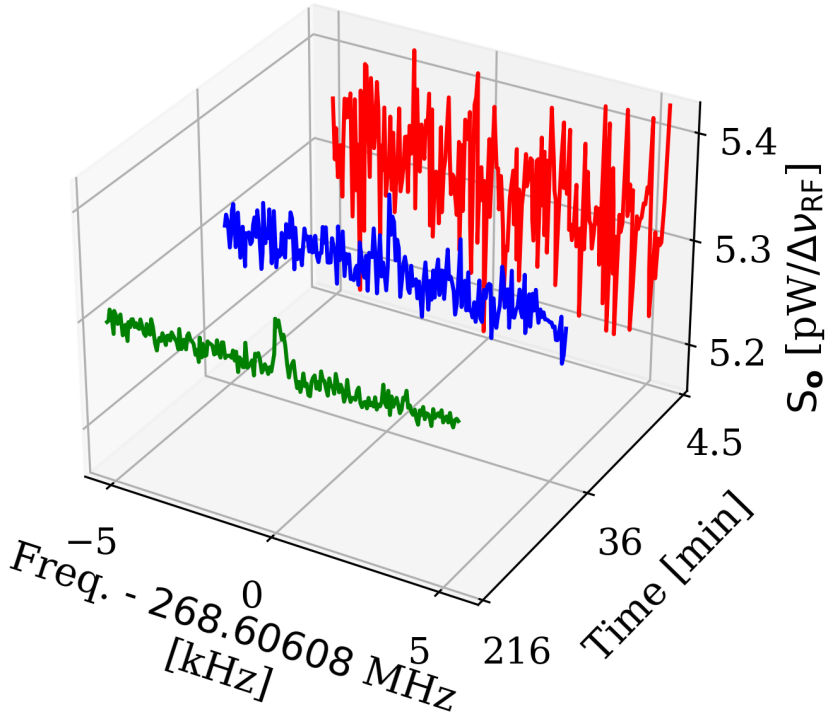


Figure 4.4: Output-referred power spectral density from the hardware injection test illustrating noise averaging down to reveal a persistent, hardware-injected, dark photon proxy signal. Spectra shown are highly zoomed around the injected frequency, 268.60608 MHz. The red, blue and green spectra represent 4.5, 36 and 216 minutes of integration time respectively. The standard deviation of these spectra (excluding the bins containing the injected signal) average down with the square root of time as expected. The blue spectrum shows the amount of averaging required for the signal to be detected by the detection algorithm (including the matched filter) at 5% significance. The tight zoom shown here is less than 1 part in 10^4 of the full 50-300 MHz spectrum analyzed.

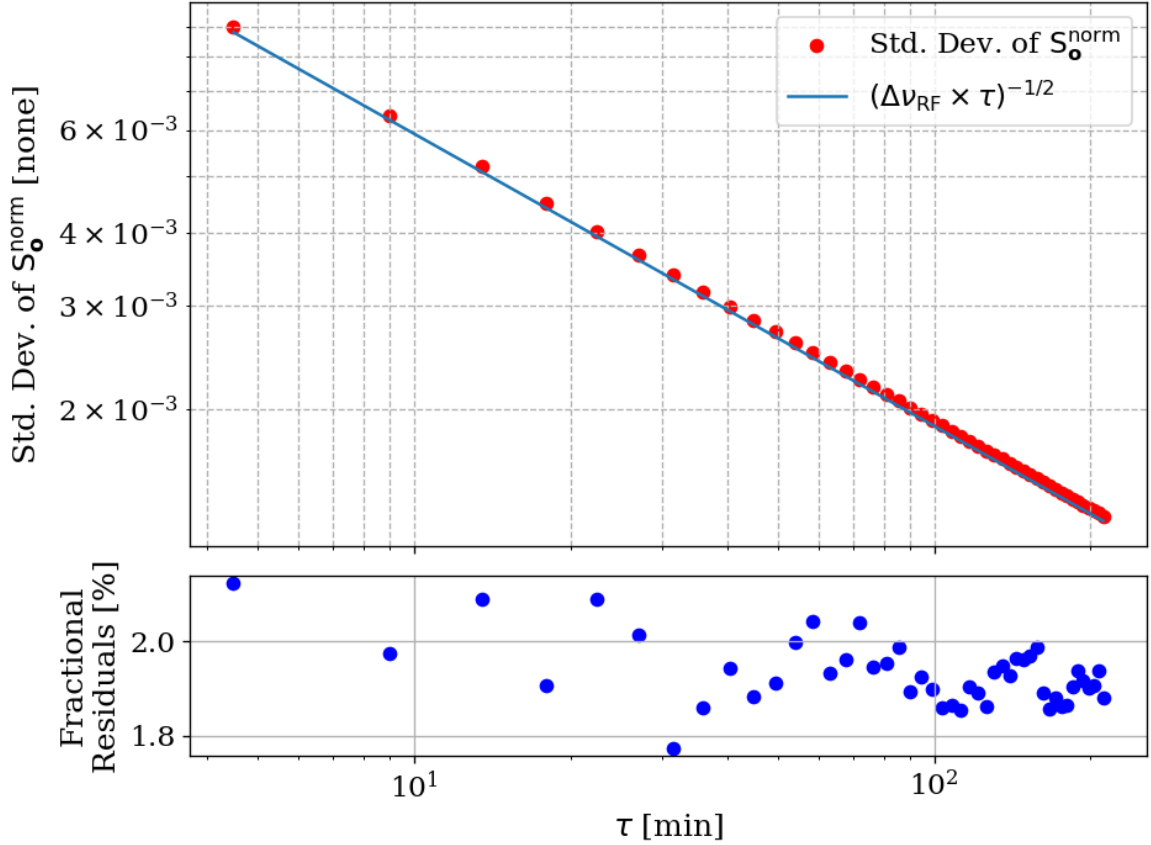


Figure 4.5: Standard deviation of output-referred power spectral density from the hardware injection test. Blue curve is the predicted standard deviation from the Dicke radiometer equation, Eq. 2.15. Each point represents 9 antenna positions with an additional 4.5 minutes of data averaged (see Sec. 4.1.2). Correlation in residuals is expected when computing the standard deviation directly, as outlined in Sec. [Analysis somewhere](#). A better fit is achieved through the median average deviation, Shown in Fig. 4.6.

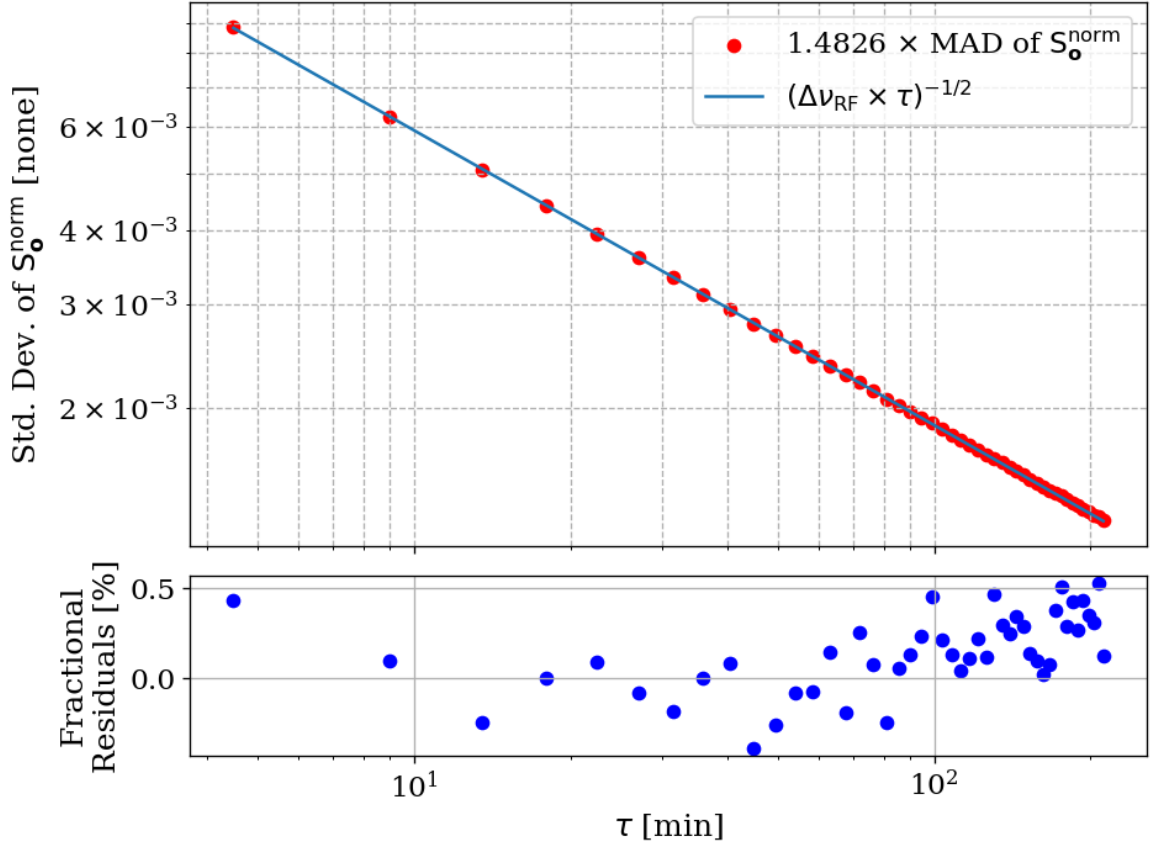


Figure 4.6: Standard deviation of output-referred power spectral density from the hardware injection test, computed with median absolute deviation (MAD). The blue curve represents the predicted standard deviation from the Dicke radiometer equation, Eq. 2.15. Each point corresponds to 9 antenna positions with an additional 4.5 minutes of data averaged (see Sec. 4.1.2). MAD provides a more robust measure of variability, reducing the influence of outliers and offering a better fit than direct standard deviation calculations, as discussed in Sec. [add reference: Analysis somewhere](#).

812 These spectra were generated one at a time and passed through the detection algorithm
 813 described in detail in Sec. [add reference: detection alg](#). The first spectrum where a signal
 814 was detected was at 36 minutes, shown in blue in Fig. 4.4. Although hardly detectable to the
 815 eye, the matched filter detects the signal with 5% significance. At the point the signal was

816 detected (i.e. before all data were averaged together), the injection frequency was confirmed
817 to have been correctly identified, resulting in a successful, blind, hardware injection test.

818 **4.1.3 Inspection of Data**

819 This subsection simply contains some full page figures which show data from the injection
820 test. They are all the same 34 minutes of data, but at different stages of processing, closely
821 following [add reference: analysis, earlier in this chapter](#). They are meant to simulate the
822 experience of inspecting a 2^{24} point FFT's power spectrum in a matplotlib widget window.
823 The zoom is seemingly unending, a feature that is difficult to appreciate in a printed docu-
824 ment. These figures should provide some context for how futile a manual search of unfiltered
825 data would be.

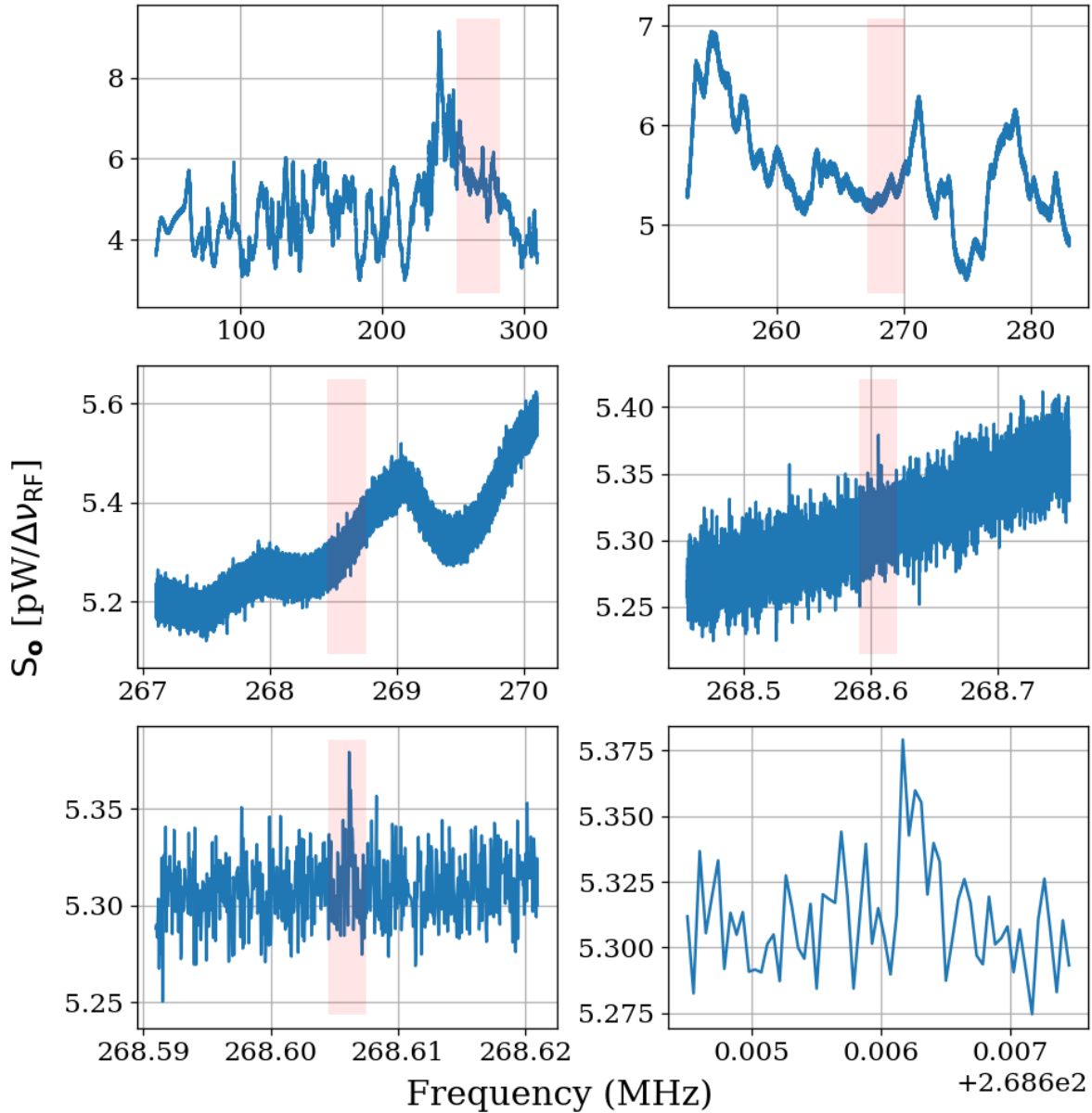


Figure 4.7: Output-referred power spectrum from hardware injection test. Injected signal at 268.60608MHz. All spectra correspond to a total of 36 minuets of averaging, split evenly between 9 antenna positions. Full 50-300 MHz span contains $\approx 5.2 \times 10^6$ bins. Light pink boxes show zoom level on following plot.

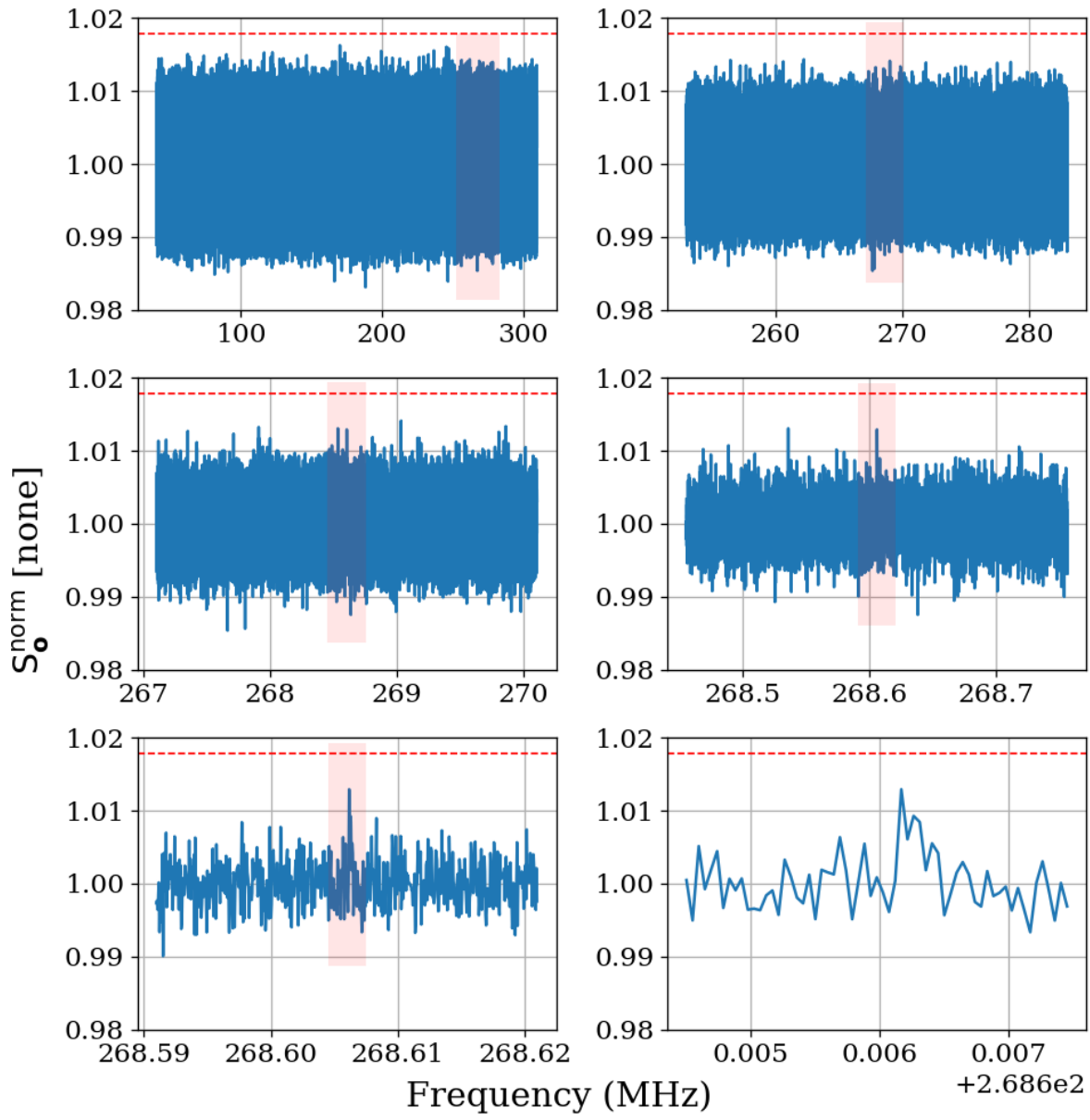


Figure 4.8: Normalized, output-referred power spectrum from hardware injection test. Injected signal at 268.60608MHz. Light pink boxes show zoom level on following plot. Red dashed line indicates the 5% significance threshold (derived in sec [add reference: end of Ch. 2](#)). Signal is not detectable above threshold.

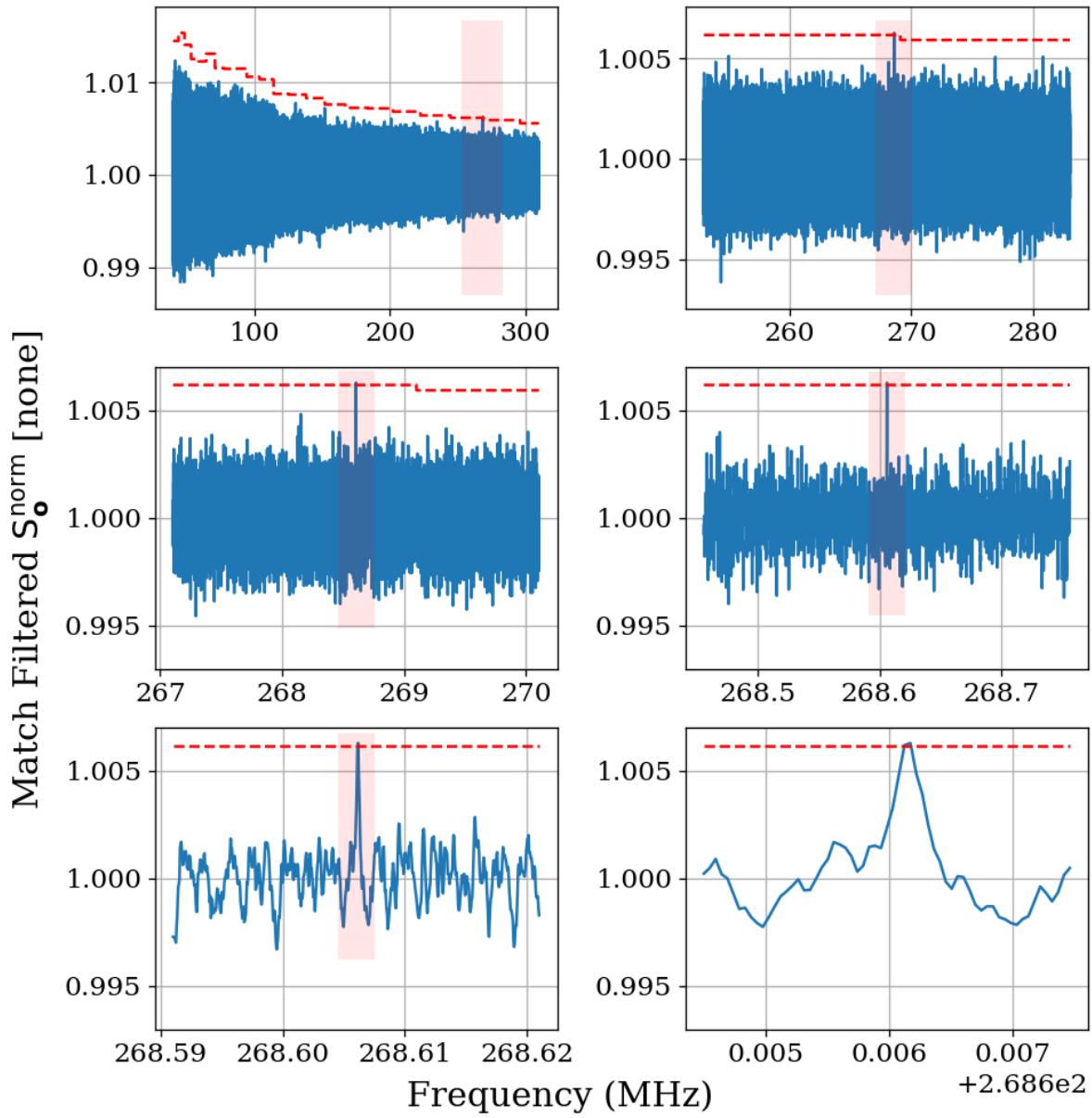


Figure 4.9: Matched filtered, output-referred power spectrum from hardware injection test. Injected signal at 268.60608MHz. Light pink boxes show zoom level on following plot. Red dashed line indicates the 5% significance threshold (derived in sec [add reference: end of Ch. 2](#)). Introducing the matched filter pushed signal above detectable above threshold.

⁸²⁶ Chapter 5

⁸²⁷ Beyond 300 MHz

To infinity and beyond!

828

Buzz Lightyear

⁸²⁹ Bibliography

- 830 [1] Fritz Zwicky. “The Redshift of Extragalactic Nebulae”. In: (1933).
- 831 [2] Vera C. Rubin and Jr. Ford W. Kent. “Rotation of the Andromeda Nebula from a
832 Spectroscopic Survey of Emission Regions”. In: (1970).
- 833 [3] Marco Battaglieri *et al.* *US Cosmic Visions: New Ideas in Dark Matter 2017: Com-*
834 *munity Report*. 2017. DOI: 10.48550/ARXIV.1707.04591. URL: <https://arxiv.org/abs/1707.04591>.
- 835
- 836 [4] V. Radeka. “Signal, Noise and Resolution in Position-Sensitive Detectors”. In: *IEEE*
837 *Transactions on Nuclear Science* 21.1 (1974), pp. 51–64. DOI: 10.1109/TNS.1974.
838 4327444.
- 839 [5] David Hill. “Plane Wave Integral Representation for Fields in Reverberation Cham-
840 bers”. en. In: 40 (1998-08-01 00:08:00 1998).
- 841 [6] W. L. Stutzman and G. A. Thiele. *Antenna Theory and Design*. John Wiley Sons,
842 1998.
- 843 [7] J.D. Kraus. *Antennas*. McGraw-Hill, 1950. ISBN: 07-035410-3.

- 844 [8] Albert Einstein. “Über die von der molekularkinetischen Theorie der Wärme geforderte
845 Bewegung von in ruhenden Flüssigkeiten suspendierten Teilchen”. In: *Annalen der*
846 *Physik* 322.8 (1905), pp. 549–560.
- 847 [9] H. Nyquist. “Thermal Agitation of Electric Charge in Conductors”. In: *Phys. Rev.* 32
848 (1 July 1928), pp. 110–113. DOI: 10.1103/PhysRev.32.110. URL: <https://link.aps.org/doi/10.1103/PhysRev.32.110>.
- 849 [10] Herbert B. Callen and Theodore A. Welton. “Irreversibility and Generalized Noise”.
850 In: *Phys. Rev.* 83 (1 July 1951), pp. 34–40. DOI: 10.1103/PhysRev.83.34. URL:
851 <https://link.aps.org/doi/10.1103/PhysRev.83.34>.
- 852 [11] C. L. Mehta. “Coherence-time and effective bandwidth of blackbody radiation”. In:
853 *Il Nuovo Cimento (1955-1965)* 28.2 (1963), pp. 401–408. DOI: 10.1007/BF02828589.
854 URL: <https://doi.org/10.1007/BF02828589>.
- 855 [12] Raphael Cervantes et al. *Deepest Sensitivity to Wavelike Dark Photon Dark Matter
856 with SRF Cavities*. 2022. arXiv: 2208.03183 [hep-ex].
- 857 [13] Alexander V. Gramolin et al. “Spectral signatures of axionlike dark matter”. In: *Physical
858 Review D* 105.3 (Feb. 2022). ISSN: 2470-0029. DOI: 10.1103/physrevd.105.035029.
859 URL: <http://dx.doi.org/10.1103/PhysRevD.105.035029>.
- 860 [14] Michael S. Turner. “Periodic signatures for the detection of cosmic axions”. In: *Phys.
861 Rev. D* 42 (10 Nov. 1990), pp. 3572–3575. DOI: 10.1103/PhysRevD.42.3572. URL:
862 <https://link.aps.org/doi/10.1103/PhysRevD.42.3572>.

- 864 [15] Greg Durgin. *Lecture on Noise Figure*. Accessed: 2024-06-23. 2017. URL: https://www.youtube.com/watch?v=M_SRUF4TQgA.
- 865
- 866 [16] Pasternack Enterprises. *PE15A1012: 1 Watt Amplifier Operating From 0.01 GHz to 6 GHz*. Accessed: 2024-05-17. 2024. URL: <https://www.pasternack.com/images/ProductPDF/PE15A1012.pdf>.
- 867
- 868
- 869 [17] SP Devices. *ADQ32 Datasheet*. Accessed: 2024-06-23. 2024. URL: https://www.spdevices.com/en-us/Products_/Documents/ADQ32/20-2378%20ADQ32%20datasheet.pdf.
- 870
- 871
- 872 [18] Benjamin Godfrey. “A Novel Search for Dark Photons”. Ph.D. dissertation. UC Davis, 2022. URL: <https://escholarship.org/uc/item/72b776v4>.
- 873
- 874 [19] L.A. Wainstein and V.D. Zubakov. *Extraction of Signals from Noise*. Englewood Cliffs, NJ: Prentice-Hall, 1962. ISBN: 9780132981330.
- 875
- 876 [20] *Series 83 RF Shielded Enclosure*. Lindgren R.F. Enclosures, Inc. 2021. URL: <https://www.ets-lindgren.com/datasheet/shielding/rf-shielding-and-accessories/11003/1100307>.
- 877
- 878
- 879 [21] David A. Hill. *Electromagnetic Theory of Reverberation Chambers*. Technical Note 1506. Gaithersburg, MD: National Institute of Standards and Technology, 1998. URL: https://tsapps.nist.gov/publication/get_pdf.cfm?pub_id=24427.
- 880
- 881
- 882 [22] D.A. Hill. “A reflection coefficient derivation for the Q of a reverberation chamber”. In: *IEEE Transactions on Electromagnetic Compatibility* 38.4 (1996), pp. 591–592. DOI: 10.1109/15.544314.
- 883
- 884

- 885 [23] Lawrence Krauss et al. “Calculations for cosmic axion detection”. In: *Physical Review*
886 *Letters* 55.17 (1985), pp. 1797–1800. DOI: 10.1103/PhysRevLett.55.1797. URL:
887 <https://doi.org/10.1103/PhysRevLett.55.1797>.
- 888 [24] “IEEE Standard Method for Measuring the Effectiveness of Electromagnetic Shielding
889 Enclosures”. In: *IEEE Std 299-1997* (1998), pp. 1–48. DOI: 10.1109/IEEESTD.1998.
890 88115.
- 891 [25] *Biconical Antenna AB-900A*. Rev. D05.19. Com-Power Corporation. May 2019. URL:
892 <https://documentation.com-power.com/pdf/AB-900A-1.pdf>.
- 893 [26] John D. Kraus. *Antennas*. 2nd. New York: McGraw-Hill, 1988, p. 892. ISBN: 9780070354227.
- 894 [27] Mini-Circuits. *ZKL-1R5: 50 Ω Gain Block Amplifier*. Accessed: 2024-06-23. 2024. URL:
895 <https://www.minicircuits.com/pdfs/ZKL-1R5.pdf>.
- 896 [28] CuPy Developers. *CuPy: NumPy-compatible array library accelerating machine learn-*
897 *ing with CUDA*. https://docs.cupy.dev/en/stable/user_guide/interoperability.html. Accessed on: May 11, 2023. 2021.
- 898 [29] Robert H Dicke. “The measurement of thermal radiation at microwave frequencies”.
900 In: *Review of Scientific Instruments* 17.7 (1946), pp. 268–275.
- 901 [30] Philippe Besnier, Christophe Lemoine, and Jerome Sol. “Various estimations of com-
902 posite Q-factor with antennas in a reverberation chamber”. In: *2015 IEEE Interna-*
903 *tional Symposium on Electromagnetic Compatibility (EMC)*. 2015, pp. 1223–1227. DOI:
904 10.1109/ISEMC.2015.7256344.

- 905 [31] R. Khatiwada et al. “Axion Dark Matter Experiment: Detailed design and operations”.
906 In: *Review of Scientific Instruments* 92.12 (Dec. 2021), p. 124502. ISSN: 0034-6748.
907 DOI: 10.1063/5.0037857. eprint: https://pubs.aip.org/aip/rsi/article-pdf/doi/10.1063/5.0037857/16136265/124502/_1/_online.pdf. URL: <https://doi.org/10.1063/5.0037857>.
- 910 [32] Yuqi Zhu et al. “An improved synthetic signal injection routine for the Haloscope
911 At Yale Sensitive To Axion Cold dark matter (HAYSTAC)”. In: *Review of Scientific*
912 *Instruments* 94.5 (May 2023). ISSN: 1089-7623. DOI: 10.1063/5.0137870. URL: <http://dx.doi.org/10.1063/5.0137870>.